Cu_2ZnSnS_4 PHOTOVOLTAICS

A Thesis
Presented to
The Academic Faculty

by

Christopher K. Tran

In Partial Fulfillment
of the Requirements for the Degree
Master of Science in the
School of Electrical and Computer Engineering

Georgia Institute of Technology
August 2019

Cu_2ZnSnS_4 PHOTOVOLTAICS

Approved by:

Dr. Jud Ready, Advisor
Georgia Tech Research Institute
Georgia Institute of Technology

Dr. John Cressler
School of Electrical Engineering
Georgia Institute of Technology

Dr. William Alan Doolittle
School of Electrical Engineering
Georgia Institute of Technology

Dr. Robert Harris
Georgia Tech Research Institute
Georgia Institute of Technology

Dr. Ajeet Rohatgi
School of Electrical Engineering
Georgia Institute of Technology

Date Approved: July 22, 2019

ACKNOWLEDGEMENTS

I would like to thank my advisor, Dr. W. Jud Ready, for his support, guidance, and advising throughout my research career since the beginning of 2017. I must also thank Dr. Brent Wagner for instruction, guidance, and sharing his wisdom in experimental procedures. Additionally, I am grateful to the past and present members of Georgia Tech Research Institute Electro-Optical Systems Laboratory (EOSL). Specifically, Stephan Turano for many trainings and advice on processing procedures early on in my career. As well as Mr. Hunter Chan, and Dr. Yuelan Zhang for their valuable advice in procedures.

I am also grateful to the graduate students and undergraduate researchers who are working in another group of Dr. W. Jud Ready and another in Dr. Eric Vogel's group. I would especially like to acknowledge Christopher Blancher for helping with some of these experiments and characterization. I would like to thank Julia Allen and Conner Awald for troubleshooting, maintaining, and fixing some tools needed for these experiments. Additionally, would also like to thank Cooper Voigt for his assistance with lab equipment and advice with some processes. Lastly, Mr. Yeyuan Yang at the IEN for his advice in processing.

Finally, I would like to acknowledge my friends and family, for the support and encouragement. I would like to thank my parents for motivating me to pursue my desired goals and to guide me into making decisions that have forever changed my life, for the better. In addition, the coffee/tea sessions in the office, with the lab-mates, which helped maintain my sanity.

TABLE OF CONTENTS

ACKNOWLEDGEMENTS iii

LIST OF TABLES vi

LIST OF FIGURES vii

LIST OF SYMBOLS AND ABBREVIATIONS x

SUMMARY xii

I Background 1
1.1 Basic Operations 2
1.2 Basic Operations 3
1.2.1 Current-voltage Curves and Circuit Models 4
1.2.2 Non-idealities 7
1.2.3 The Thickness and Absorption Trade-off 10
1.3 Three Generations of Photovoltaics 10
1.3.1 Generation I 11
1.3.2 Generation II 11
1.3.3 Generation III 13
1.4 Absorber Layer 14
1.5 Molybdenum Back Contact 14
1.5.1 Trade-offs of Mo 15

II Experimental Design 17
2.1 Deposition Methods 17
2.1.1 Ion Assisted Deposition 18
2.1.2 Sputtering 18
2.1.3 Molecular Beam Epitaxy 19
2.2 Molybdenum Back Contact 19
2.3 CZTS Absorber Layer 20
2.4 Thermal Anneal Sulfurization 21
2.5 CdS Window Layer 22
2.6 ZnO High Resistance Transparent Layer 23
2.7 ITO Transparent Conductive Oxide 23

III Experimental Procedure 24
3.1 Cleaning 24
3.2 Molybdenum Deposition 24
3.3 Sputtering of CZT 25
3.4 Sulfurization and CdS 26
3.5 ZnO and ITO Deposition 28

IV Results 30

4.1 Molybdenum Deposition 30
4.2 CZT Deposition 31
4.3 CZTS Sulfurization 34
4.3.1 Temperature 36
4.3.2 Impact of plasma 38
4.3.3 Flow Rate 38
4.3.4 Addition of Soft Anneal Step 39
4.3.5 Higher Pressure Sulfurization 43
4.4 CdS Deposition 45
4.5 ZnO Deposition 46
4.6 ITO Deposition 47
4.8 CZTS Cells 48
4.9 Summary of Results 50

V Summary and Future Work 52
5.1 Summary of Contributions 52
5.2 Future Work 52

Appendix A. Tables of Deposition Parameters 54
A.1 Deposition of Mo 54
A.2 Deposition of CZT 55
A.3 Sulfurization of CZT 57
A.4 MBE Deposition of CdS 61
A.5 MBE Deposition of ZnO 62
A.6 MBE Deposition of ITO 63

REFERENCES 65

LIST OF TABLES

Table 1	Plasma and electron beam gun parameters for ZnO and ITO deposition.	29
Table 2	Table of parameters and of CZT sputter deposition.	31
Table 3	Comparison between the composition of deposited CZT and the CZT sputter target.	34
Table 4	Sulfurization process parameters and its respective EDS composition of CZTS. The temperature, time, flow of H_2S, and pressure are the parameters changed. A soft temperature anneal of 350 °C was added to some of the later runs.	35
Table 5	Sheet resistance and Resistivity of ITO samples with change in oxygen flow during the process.	46
Table 6	ZnO depositions parameters and resistivity.	47
Table 7	CZTS PV Cells showing deposition parameters and performance characteristics.	49
Table 8	IAD deposition of Mo.	54
Table 9	Evovac CZT deposition parameters.	55
Table 10	MBE sulfurization parameters.	57
Table 11	MBE CdS deposition paramters.	61
Table 12	IAD ZnO deposition parameters.	62
Table 13	IAD ITO deposition parameters.	63

LIST OF FIGURES

Figure 1	Standard IV curve of a solar cell.	5
Figure 2	Solar cell equivalent circuits.	6
Figure 3	Effects of increasing and decreasing series and shunt resistances.	7
Figure 4	Types of carrier recombination mechanisms that occur in a semiconductor.	8
Figure 5	The fill factor (left) and open-circuit voltage (right) of sputtered CZTS is lacking compared to CIGS, CdTe, and c-Si [21].	9
Figure 6	Three generations of solar cells comparing efficiency and cost per Watt.	11
Figure 7	(Left)Design of 2D CZTS PV. (Right) Top view of 2D CZTS PV.	17
Figure 8	Efficiency, Fill Factor, V_{OC}, and $J_{S\ C}$ vs Mo Thickness [37].	19
Figure 9	Voltage vs current density of CZTS solar cells varying pressure [48].	21
Figure 10	CZTS thickness vs Efficiency [20].	21
Figure 11	Contour plot of CdS:CZTS efficiency as a function of their corresponding thicknesses [13].	22
Figure 12	(Top left) Exterior of Leybold IAD system. (Top right) Interior view of Leybold IAD system. (Bottom) Schematic of IAD components.	25
Figure 13	System used to sputter CZT.	26
Figure 14	MBE system used to sulfurize CZT and deposit CdS.	27

Figure 15	CdS BEP vs cell temperature from beam flux testing.	28
Figure 16	Sheet resistance of molybdenum vs thickness.	30
Figure 17	SEM micrograph of Mo deposited using the Leybold APS 1104 electron beam gun.	31
Figure 18	SEM micrographs of CZT samples.	33
Figure 19	CZTS composition of different sulfurization parameters.	35
Figure 20	Energy-dispersive X-ray spectroscopy (EDS) focused on the crack formations on the surface of the CZTS layer.	36
Figure 21	SEM micrograph of sulfurization processes done at 510 °C.	37
Figure 22	EDS analysis on CZTS without the use of plasma.	38
Figure 23	SEM micrographs of CZTS with and without a soft anneal sulfurization.	39
Figure 24	EDS analysis of a CZTS sulfurization sample with the addition of a soft anneal step at 350 °C prior to the hard anneal step of 510 °C.	40
Figure 25	Surface defects exhibited by adding a soft anneal process.	41
Figure 26	SEM micrograph of the cross section of sulfurized CZT	42
Figure 27	EDS mapping of Sulf_11 sample.	43
Figure 28	SEM micrographs showing the formation of surface fissures at higher process pressures.	44
Figure 29	Temperature required each run to maintain the same BEP of 3.0×10^{-6} torr.	45
Figure 30	Transmittance spectrum of ZnO.	46

Figure 31 Transmittance spectrum of ITO samples compared to soda lime glass as the baseline. 48

Figure 32 IV curve of three CZTS PV cells. 49

LIST OF SYMBOLS AND ABBREVIATIONS

AM	Air Mass
a-Si	Amorphous Silicon
BEP	Beam Equivalent Pressure
CdS	Cadmium Sulfide
CdTe	Cadmium Telluride
CNT	Carbon nanotube
CIGS	$CuIn_{1-x}Ga_xSe_2$
CZT	Copper Zinc Tin
CZTS	Cu_2ZnSnS_4
EDS	Energy Dispersive Spectroscopy
eV	Electron volts
FF	Fill Factor
GW	Gigawatt
H_2S	Dihydrogen Sulfide
HRT	High Resistance Transparent
IAD	Ion assisted deposition
ITO	Indium Tin Oxide
IV	Current-Voltage
J_m	Max current density
J_{sc}	Short-circuit current density
L_{diff}	Diffusion length

MBE	Molecular Beam Epitaxy
Mo	Molybdenum
P_{mp}	Max power point
P_s	Incident power density
PV	Photovoltaics
RF	Radio Frequency
R_{sheet}	Sheet Resistance
SEM	Scanning Electron Microscope
SLG	Soda Lime Glass
Si	Silicon
SRH	Shockley-Read-Hall
TCO	Transparent Conductive Oxide
TW	Terawatt
V_m	Max voltage
V_{oc}	Open-circuit voltage
W	Watt
Wh	Watt-hour
XRD	X-ray Diffraction
ZnO	Zinc Oxide

SUMMARY

Photovoltaics (PVs) can be a phenomenal source of green energy that has the potential to outperform fossil fuels in cost and efficiency. This work concentrates on developing efficient thin film PVs with abundant and environmentally friendly materials, such as Cu_2ZnSnS_4 (CZTS).

There have been many studies and reviews on different deposition techniques and parameters for fabricating CZTS PVs. This research focuses on exploring and integrating optimal reported thicknesses of materials to fabricate higher efficiency CZTS cells. Additionally, this research focuses on process development of fabrication methods for the layers in the PV stack as well as exploring the use of plasma assisted dihydrogen sulfide to fabricate the absorber layer. These parameters include thicknesses, annealing temperatures and times, processing pressures, and operating power. The integration of optimal reported processing parameters and techniques allow the improvement of the device performance.

In this research, molybdenum was used as the back contact, CZTS as the absorber layer, CdS as the window layer, ZnO as the passivation layer, and ITO as the top contact. The deposition of Mo on glass as the back contact was done by electron beam evaporation for 200 nm. CZTS was deposited by sputtering 1.3 μm of CZT and using H_2S to sulfurize the CZT for 30 minutes. CdS was deposited by molecular beam epitaxy for 20 nm. ZnO and ITO are both deposited using a plasma assisted electron beam deposition for 20 nm and 150 nm respectively.

Electron beam deposition of molybdenum was found to be acceptable as the back contact of the solar cell. The deposited molybdenum resulted in a smooth and uniform layer. The sheet resistance (R_{sheet}) of the molybdenum was 15.31 ± 0.2 Ω/□ for approximately 200 nm.

The deposited 1.3 μm of CZT by sputtering was problematic when continuously depositing the material. This caused the backing plate of the target to separate from the material. Additionally, when separated, the deposited CZT layer was less dense and contained more voids. A superior layer was deposited when the deposition was cycled between deposition and cooling phases. The cycled deposition resulted in greater density and a more uniform layer of sputtered CZT.

The use of H_2S to sulfurize CZT was attempted to form the absorber layer CZTS. The sulfurization process resulted in surface deformities and sulfur deficient absorber layer. Longer annealing times in an H_2S environment resulted in zinc poor structures. However, a soft anneal step before the hard anneal shown to stabilize the zinc concentration, but resulted in surface deformities. Although the composition of the sulfurized CZT layer was not stoichiometrically equivalent, it may be possible to achieve such a ratio using this method.

The deposited 20 nm ZnO as a passivation layer was shown to be significant for the created PV cells. This is to passivate any electrical pathways that may exist through the CZTS absorber layer. The performance of the fabricated PV cells were significantly increased when the ZnO layer was present. Additionally, this thin film was measured to have a transmittance of above 95% for wavelengths of 350-1050 nm.

The 150 nm of ITO deposited as the top contacted exhibited an R_{sheet} of 25-30 Ω/□. The increased flow of oxygen during the deposition resulted in an increase of transmittance, but in exchange, sacrificing conductivity. The ITO film resulted in transmittances of 80% and higher for wavelengths of 350-1050 nm.

A total of 3 PV cells were fabricated. However, the cells had very low performance due to its incomplete CZTS structure. Ideally, the p-type absorber, CZTS structure should be $Cu_{25}Zn_{12.5}Sn_{12.5}S_{50}$ (atomic %) in order to have 1.5 eV bandgap. The fabricated CZTS layer resulted in low zinc and sulfur content. Hence, the performance of these cells behaved similar to light sensitive resistors instead of diodes. Results show that a ZnO layer was crucial in increasing the performance of the cell. Additionally, a zinc deficit CZTS layer, caused by a long annealing time, results in very low performance.

I BACKGROUND

PVs have become an increasingly popular source of renewable energy for reducing pollution due to its inexhaustible supply. In 2017, the leading source of energy for the US was fossil fuels, amounting to 62.7%, with solar energy being 1.3%, of the total energy generation [1]. Solar energy, a significant energy source for some countries, is underutilized in the US due to having less permitting and installation processes and protocols for PV systems [2]. In 2017, the global solar capacity increased by almost 100 GW of power to 402 GW, a capacity increase of one-third [3]. Barriers such as low efficiency, low throughput of higher efficiency cells, and high cost cause solar energy to be undesirable. If solar technology overcame these barriers, it could provide new jobs, allow for technological advancements, and eventually eliminate environmentally detrimental sources of energy.

On average, 174.7 W/m^2 of solar flux strikes the earth's surface, resulting in the theoretical potential of solar power of 89,300 TW (over 220,000 times of the global solar capacity in 2017) [4]. Global power consumption is 18 TW on average, so if 0.02% of the potential solar power impinging on the earth's surface was harvested, this would be enough to replace all the other energy sources in the world [5]. High efficiency solar cells are expensive to fabricate and require more research and development to make cheaper. However, with solar energy costing around \$0.03/ kWh and fossil fuels costing \$0.05 kWh, the U.S. can save approximately \$53 billion dollars annually if fossil fuels were to be replaced with solar energy [1].

Unlike the dependence on fossil fuels on earth, PV technology has been the main source of power for space-based applications. Such devices require the most efficiency possible per solar cell due to limitations on weight and surface area of mountable cells. The price of solar cells is insignificant compared to the price of satellite and launch. For space applications, research on solar cells with high efficiency and low mass are prioritized over cost. There are many factors that can improve the performance and cost of PVs. These include the addition of antireflective coatings, the integration of materials in the absorber and window layers, the material of the electrodes, and the inclusion of light-trapping textured surfaces.

1.1 Basic Operations

The PV effect was first discovered by Becquerel in 1839 when he exposed a silver chloride electrode to light, inducing an electrical current [6-8]. In 1873, selenium was the first material discovered to be photoconductive by W. Smith [9]. With the work of Hertz and Einstein, the photoelectric effect is first observed and explained respectively in 1905 [10], which led to the development of the first PV devices.

Physicists at Bell Labs implemented the first PV device produced for space applications in 1950 [7]. In 1954, the first single crystal silicon solar cell with 6% efficiency was made at Bell Labs which was later increased to 8% with the patents of Pearson, Chapin, and Fuller [7, 11]. This marked the beginning of implementing commercially available renewable energy into the market of electricity. The first PV system for terrestrial applications was implemented to power a rural carrier telephone communication system located in Americus, Georgia in 1955 [12].

1.2 Basic Operations

Solar cells operate by using a charge separation mechanism, typically a p-n junction, or a series of junctions, to generate voltage. A p-n junction is made by joining a p-type semiconductor directly with an n-type. A p-type semiconductor is doped with electron acceptor atoms, and an n-type is doped with electron donor atoms. This creates a space charge region or depletion region between semiconductors where free charge carriers are non-existent due to an electric field.

When an individual photon of light penetrates the n-type emitter region, an electron from the valance band may be excited by the energy of the photon upon collision. In order for the valance electron to be promoted, the energy of the photon needs to be greater than the bandgap of the semiconductor material. The loss of a valance electron gives rise to a hole resulting in the generation of an electron-hole pair. The electric field formed by the emitter and base regions allows the free electron to drift and the concentration gradient allows the minority carrier holes to diffuse, resulting in a separation of charge. Holes, as the minority carrier in the emitter region, need to diffuse to the depletion region to be collected. For a higher chance of collection, the emitter region needs to be very thin, theoretically less than 40 nm [13], to lower chances of recombination from grain boundaries, or dislocations. If the photon is absorbed in the p-type base region, an electron hole pair can also be generated. The electron, as the minority carrier in this region, needs to diffuse to the depletion layer. Because the concentration of holes in the base region is greater than electrons, the thickness of the region is less relevant, where electrons can diffuse for several diffusion lengths.

1.2.1 *Current-voltage Curves and Circuit Models*

The current-voltage (IV) curve characterizes the efficiency of both a diode and a solar cell. Without illumination, an ideal solar cell behaves exactly like a diode. However, for solar cells, a current is produced when exposed to light. This generation in current results in the diode curve to move into the fourth quadrant due to the nature of the electric field of the space charged region in the p-n junction. The intersections at the x and y axes of an IV curve are defined to be the open-circuit voltage (V_{oc}) and the short-circuit current density (J_{sc}) respectively (Figure 1 left). The max current density (J_m) and max voltage (V_m) the device can achieve is found at the max power point (P_{mp}) (Figure 1 right).

The fill factor (FF) is defined as a ratio between P_{mp} and the theoretical max power of an ideal cell. This is defined as

$$FF = \frac{P_{mp}}{V_{OC} * I_{SC}}. \quad (1)$$

FF may be used to calculate the efficiency (η) of solar cells, which is the ratio between the power density delivered at the operating point to the incident power density, P_s, can be defined as

$$\eta = \frac{J_{sc} * V_{oc} * FF}{P_s}. \quad (2)$$

The FF for a diode defines the sharpness of the IV curve, where ideally should be at the intersection between the J_{sc}, and V_{oc} (Figure 1). A solar cell is typically characterized by the parameters V_{oc}, J_{sc}, FF, and η, using a standard testing intensity of 1000 W/m^2 or Air Mass (AM) 1.5.

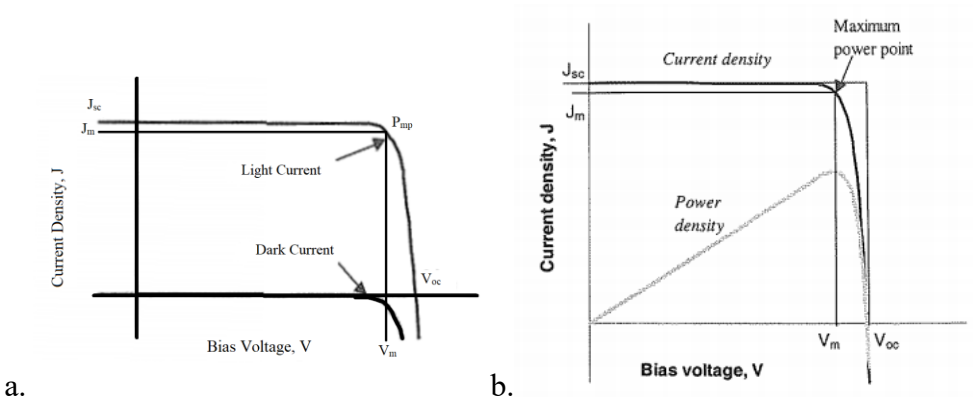

Figure 1 – (Left) Standard IV curve of a solar cell. Showing light and dark current of the device. (Right) The curves shown include an ideal maximum power point, non-ideal maximum power point, and a power density. From [14]. Additionally, the parameters of V_{oc}, J_{sc}, and P_{mp} are shown on the curves.

The equivalent circuit of an ideal solar cell includes a current source in parallel with a diode (Figure 2 left). The current source represents the current generated by light and the diode in parallel drives the photocurrent through a connected load. In practice, there are no solar cells that are ideal. Therefore, the equivalent circuit for a non-ideal solar cell includes resistances and leaky diodes (Figure 2 right).

The non-ideal solar cell can be modelled as a circuit by a current source, two leaky diodes, shunt resistance (R_{Sh}), and series resistance (R_s) shown in Figure 2 (right). The series resistance originates from the cell bulk material, contacts, and sheet interconnection. Shunt resistance arises from leakage of current through the cell, crystal defects in the junction, and around the edges of the device [14].

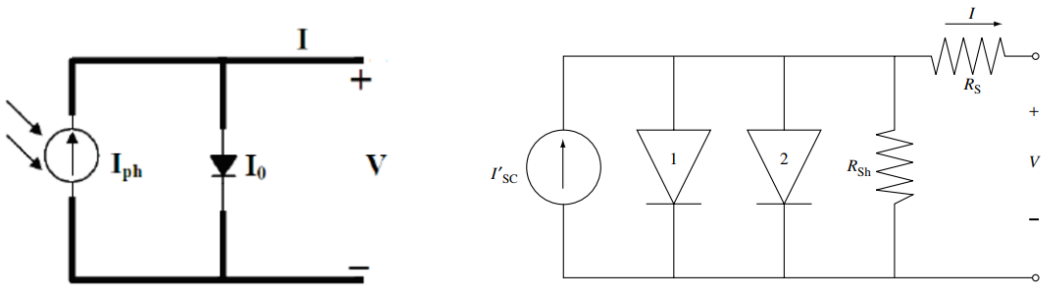

Figure 2 – (Left) An ideal solar cell equivalent circuit. This includes a photocurrent source I_{ph} parallel to a diode, from [15]. (Right) Equivalent circuit of a non-ideal solar cell. The circuit contains a current source, I_L, two leaky diodes, 1 and 2, and series and shunt resistors (R_S and R_{Sh}). The first diode, 1, refers to recombination current in the quasi-neutral regions. The second diode, 2, refers recombination current in the depletion region. R_s refers to the intrinsic resistance from the bulk and contact materials. R_{Sh} refers to the shunting from contacts to the defects in the material [16].

For a non-ideal solar cell, the net current density in the cell is defined as

$$J = J_{sc} - J_o\left(e^{\frac{qV}{k_b}} - 1\right), \tag{3}$$

where J_0 is the dark saturation current density, q is the electron charge constant, V is the applied voltage across the terminals, and k_b is Boltzmann's constant.

The fill factor is reduced when R_S increases and R_{Sh} decreases (Figure 3). For an ideal cell, R_S is zero, and R_{Sh} is infinite to maximize the current provided to a load.

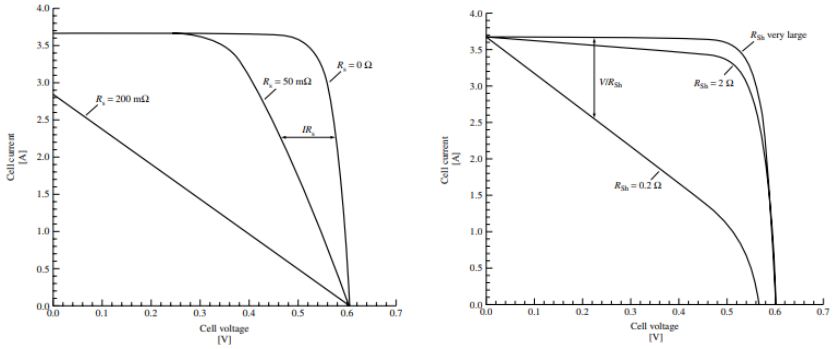

Figure 3 – Effects of increasing and decreasing series resistance (left) and shunt resistance (right) of the IV curvature of a solar cell. For maximum fill factor, R_{Sh} must be very large and R_S is very small. From [16].

1.2.2 *Non-idealities*

Solar cells inherently have defects that directly affect their performance. At a lower level, electron-hole recombination can greatly affect the output of a cell. There are three types of recombination in solar cells: (1) radiative recombination, (2) Auger recombination, (3) Shockley-Reed-Hall (SRH) recombination.

Radiative recombination (Figure 4 left) is a process that occurs inherently in any p-n junction. This process can be seen as the reverse of absorption, where high-energy electrons return to a lower energy state resulting in the emission of a photon. This recombination accounts for a small percentage of photons in a cell that are emitted and is commonly used with light emitting diodes.

Auger Recombination (Figure 4 middle) is similar to radiative where an electron recombines with a hole, or vice versa, but instead the excess energy is used to promote a hole or electron to a higher energy level. The excess energy from the elevation is distributed by lattice thermalization. The effect of this recombination decreases strongly with increasing bandgap [17].

SRH recombination (Figure 4 right) occurs when an electron or hole recombine through traps or defects within the bandgap. These traps originate from impurities, defects, and dislocations in the material. The energy produced from the recombination is released as a lattice vibration throughout the semiconductor as a phonon.

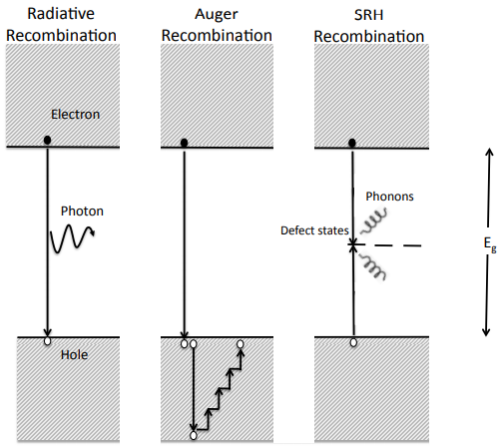

Figure 4 – Types of carrier recombination mechanisms that occur in a semiconductor. The upper band is shown as the conduction band and the lower band as the valence band. Radiative recombination, Auger recombination, SRH recombination are shown from left to right respectively. Radiative recombination occurs when an electron in the conduction band is demoted and combines with a hole in the valence band. Auger recombination occurs when an electron recombines with a hole with excess energy, resulting in lower energy carrier to be promoted to a higher energy level. SRH recombination occurs when a carrier becomes trapped in a defect state, between conduction and valence band, which emits phonons as a result of energy loss. From [18].

In CZTS, the Sn and Cu anti-site defects are too shallow or too deep to act as efficient electron-hole recombination centers [19]. The efficiencies of CZTS films are mainly limited by its low fill factor and low open-circuit voltage shown in Figure 5. This is due to recombination in the bulk and CZTS/CdS interface, as well as, very high density defects contributing to low energy radiative recombination [20]. Differences in quality of the material of the absorber layer and the interface layer between the absorber layer and

buffer layer may contribute to recombination losses. In order to form high quality CZTS films, it is crucial to have high control of the film composition as well as sulfurization parameters [21].

Light absorption may be optimized by having a thicker layer of CZTS, but only if the film quality is optimal. Dhakal et al. reported a 6.2% efficient cell with 1.3 μm CZTS layer, but found that the diffusion length was 350 nm [22]. Only 350 nm was contributing to the electron hole pair generation due to defect states and secondary phases within the CZTS material. The low bandgap secondary phases, such as Cu_2S, SnS, and Cu_2SnS_3, result in reduced carrier collection efficiency, and enhanced carrier recombination [20, 21].

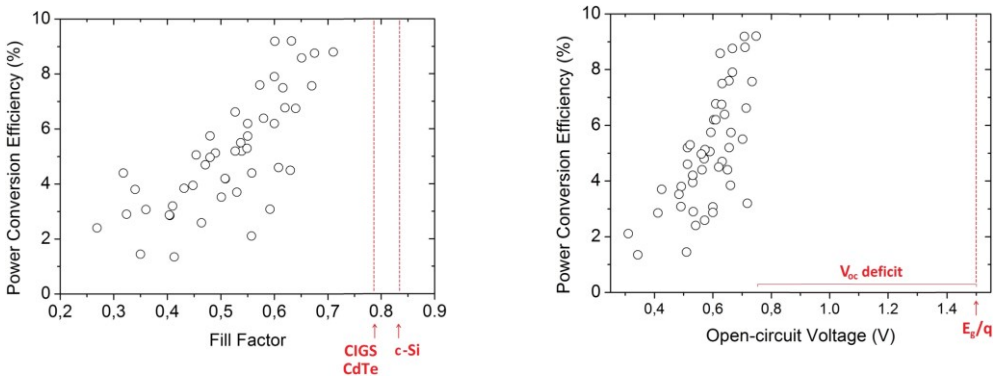

Figure 5 – The fill factor (left) and open-circuit voltage (right) of sputtered CZTS is lacking compared to CIGS, CdTe, and c-Si. From [21].

Defect states and defect complexes such as vacancies, interstitials, and antisites, may be present and lead to lower diffusion lengths if the quality of the CZTS film is not optimal.

Efficiency can be highly reduced by several loss mechanisms introduced with PV. These can be categorized into two categories: (1) Optical and (2) Electrical. Optical losses consist of heat, absorption, reflection, shadowing, and incomplete absorption, which can be reduced by minimizing contacts to reduce reflection and shadowing. The bandgap of

the material determines the heat loss and the absorption. Electrical losses originate from the thickness of materials and are optimized by using thinner materials to lower the chances of recombination.

1.2.3 *The Thickness and Absorption Trade-off*

There exists a trade-off in performance between absorption and thickness when it comes to thin film solar cells. The photo absorber must be thick to maximize the absorption of photons, but thin enough to reduce carrier recombination. The thicker the photo-absorber layer, the greater the absorption, but the longer the pathway for carrier diffusion and extraction. In order to optimize the performance of a thin-film cell, a solution may be to utilize textured structures from patterned carbon nanotubes (CNTs) to increase the probability of absorption through light trapping while maintaining a thin absorber layer of CZTS for a shorter pathway for carriers to diffuse.

1.3 Three Generations of Photovoltaics

Today, solar cells are separated into three distinct generations: I) Silicon, II) Thin film, III) Organic. These generations can be separated by their cost per Watt and overall efficiency shown in Figure 6.

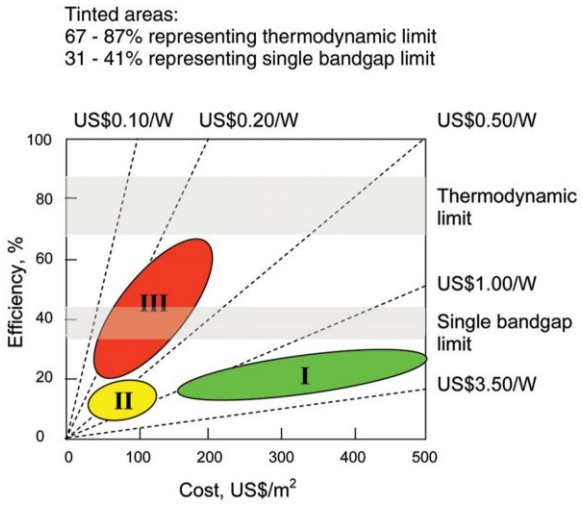

Figure 6 – Three generations of solar cells comparing efficiency and cost per Watt. Generations being wafer-based, thin films, and advanced films as I, II, and III respectively. The thermodynamic limit explains the maximum energy produced from incident solar energy. The single bandgap limit explains the maximum efficiency a single bandgap device can achieve. From [23].

1.3.1 *Generation I*

Silicon based cells, which account for 86% of the market, dominate in performance but suffer from high manufacturing cost [24]. The high purity single crystal silicon contains low defects which leads to lower recombination losses in the material and higher carrier lifetime, contributing to high efficiencies and high cost. These cells have an efficiency of around 26% today [25]. However, silicon is an indirect bandgap material and requires a thicker layer, around 50-100 μm [26], to compensate for its low absorption coefficient.

1.3.2 *Generation II*

Generation II contain thin film cells such as $CuIn_{1-x}Ga_xSe_2$ (CIGS), amorphous Si (a -Si), cadmium telluride (CdTe), and Cu_2ZnSnS_4 (CZTS) among others. Thin film cells are much more cost effective than Si, though they lack the efficiencies that first generation devices achieve.

CIGS

CIGS solar cells have been able to achieve efficiencies of 20.3% on rigid glass substrates [27]. The bandgap of this material can be varied from 1-1.6 eV [28]. Typically, CdS is chosen as the n-type buffer layer and paired with the p-type CIGS absorber layer. The overall thickness of a CIGS cell is 1.2 μm as opposed to the 170 μm crystalline silicon cells [28].

Amorphous Silicon

Amorphous Si (a-Si) cells have a bandgap of 1.75 eV with stabilized efficiencies up to 13.6% in 2015 by Sai et al [28]. These cells typically require hydrogen passivation to achieve higher efficiencies due to the dangling bonds from the structure. However, the hydrogen bonds can be broken at elevated temperatures (greater than 130 °C) by irreversible light-enhanced diffusion of hydrogen, making them unsuitable for long term applications [29].

CdTe

CdTe solar cells have a bandgap of 1.44 eV with efficiencies up to 21.1% by First Solar Research and Development [28]. The p-type CdTe is typically paired with an n-type CdS buffer layer. Through the use of vapor transport deposition, First Solar was able to continuously achieve the world record for CdTe single junction thin film cells [28].

CZTS

CZTS is a popular material for the direct bandgap absorber layer because of desirable properties such as a relatively high absorption coefficient $10^4 cm^{-1}$, an optical bandgap of 1.5 eV, high abundancy, and nontoxicity [21, 22, 30-33]. CZTS PV have the potential to reach 28% efficiency according to the Shockley-Queisser limit [21, 22].

The efficiencies of CZTS has been relatively low compared to CIGS and CdTe thin-film solar cells. The record CZTS cell was a CZTSSe cell achieved a power conversion efficiency of 12.6% in 2014 [34, 35]. However, the cell was fabricated using a hydrazine-based pure solution, which is a highly reactive and toxic approach.

The champion CZTS cell with a 11.01% efficiency was reported by Yan with a V_{oc} of 730.6 mV and a J_{sc} of 21.74 mA cm^{-2} [36]. The fabrication process reported by Yan is as follows: The CZTS layer was co-sputtered using Cu/ZnS/SnS targets to deposit a total thickness of 500 nm on top of Mo coated glass. Then the sample was sulfurized through rapid thermal processing at 560 °C for 3 minutes in a combined sulfur and SnS atmosphere. Chemical bath deposition was used to deposit 50 nm of CdS. A heterojunction heat treatments was conducted at various temperatures in a tube furnace. A very thin layer of ZnO was deposited approximately 55 nm. Lastly, the ITO layer, 240 nm, was deposited on top with an R_{sheet} of 30 Ω/□.

1.3.3 *Generation III*

Generation III devices include devices that consist of concentrator cells, thin film tandem cells, and organic cells. This generation aims to lower the cost of PV down to

$0.20/W or lower by increasing efficiencies while maintaining cost advantages of thin-film deposition techniques [23]. To achieve greater efficiencies, the Shockley-Queisser limit must be achieved. The use of multiple energy threshold devices, or the use of tandem technology, can be used to achieve higher efficiency devices.

1.4 Absorber Layer

The quality of the absorber layer material is typically characterized by its minority carrier diffusion length (L_{diff}). It is known that a short L_{diff} results in a lower short-circuit current J_{sc} and V_{oc} of a device shown in Eqs. (4), (5) [21]. The thickness of the absorber layer is limited by the L_{diff} of the material. Light absorption can be increased by having a thicker absorber material, which requires a longer L_{diff}.

$$J_L \propto q g_o L_{diff} \tag{4}$$

$$V_{oc} = \frac{E_g}{q} - \frac{A k_B T}{q} \ln\left(\frac{J_{00}}{J_L}\right) \tag{5}$$

where, J_L is the illuminated current density, q is the electron charge, g_o is the optical generation rate; E_g is the bandgap; A is the diode ideality factor; k_B is the Boltzmann constant; T is the temperature; and J_{00} is the weakly temperature-dependent prefactor [21].

1.5 Molybdenum Back Contact

Molybdenum is widely used as back contacts for CZTS solar cells due to its low resistivity (6.35×10^{-5} Ω-cm [37]), low R_{sheet} (1-2 Ω/square [38]), and good adhesion to soda lime glass substrates [37, 39, 40]. The higher density of Mo contributes to the lower

R_{sheet} due to fewer traps in the material. Resistivity seems to stay constant with varying thicknesses, while higher R_{sheet}, series resistance, and fill factor are reported at lower thicknesses of Mo [38].

1.5.1 *Trade-offs of Mo*

The formation of MoS_2 when CZTS was thermally processed was found to be dependent with annealing times of CZTS; it introduced a lower bandgap secondary phase at the CZTS/Mo interface[41, 42]. The secondary phase may contribute to bulk recombination of charge carriers in this interface. The longer the annealing time of CZTS, the greater the thickness of MoS_2 is formed. The defects from the backside may diffuse into the bulk of the semiconductor to cause detrimental losses. Additionally, MoS_2 has an electrical conductivity of 10^{-4} S/cm [43] , which is an nine orders of magnitude less than that of Mo. This introduces significantly high losses from unwanted resistance.

Although, out-diffusion of Mo into CZTS from higher sulfurization temperatures will decrease the series resistance and increase the shunt resistance of the PV cell by reducing recombination centers at the interface [41]. The reduction of recombination centers allows for a longer carrier lifetime, which contributes to efficiency improvements. The benefits from the out-diffusion of Mo into CZTS seems to outweigh the detrimental nature of MoS_2.

The out diffusion of sodium from the soda lime glass, through the Mo, and into the CZTS may be beneficial for the device [38, 44]. However, certain problems may arise if the thickness of Mo is too excessive or underwhelming. If the Mo is too thin, the out-diffusion of sodium from the soda lime glass may be serious. A thin Mo layer was shown

to increase in series resistance and reduce fill factor; when too thick, the sodium concentration in the next film grown on top of the contact will result in a lower V_{oc}. [38]. The optimal thicknesses of Mo for the CIGS cells fabricated by Kimikawa et al. were found to be 200 nm [38].

II EXPERIMENTAL DESIGN

The stack of the PV cell consists of a 3 mm thick soda lime glass as the substrate, Mo back contact, CZTS absorber layer, CdS window layer, ZnO, TCO (transparent conductive oxide), and the top contact ITO. The stack is shown in Figure 7. This section explains the significant contributions of each layer in the solar cell stack.

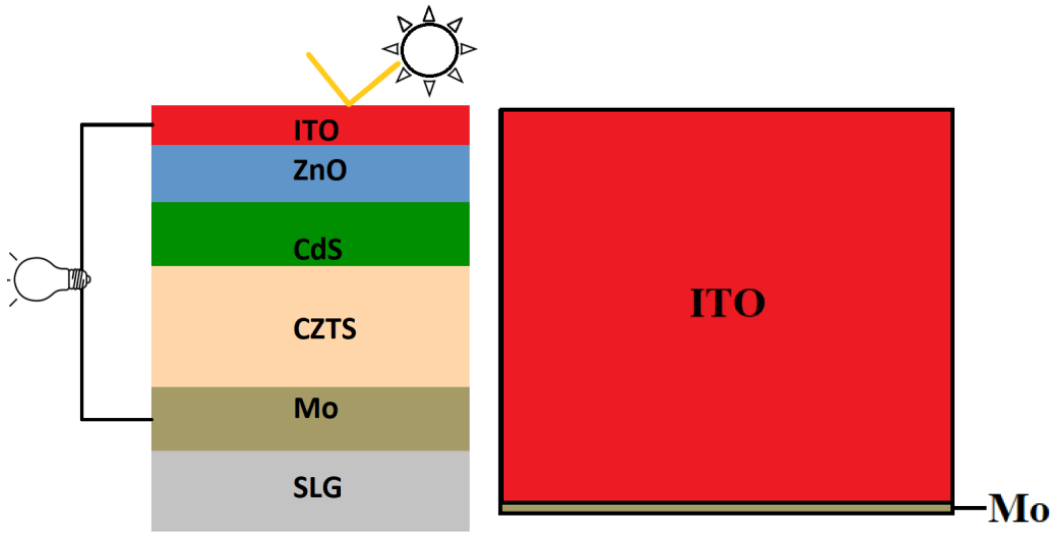

Figure 7 – (Left) Design of 2D CZTS PV. (Right) Top view of 2D CZTS PV.

The proposed research will include: (1) the investigation of the optimal thicknesses of each material in the CZTS solar cell stack, (2) the process development to deposit each layer.

2.1 Deposition Methods

The first component entails the method of deposition of Mo, CZTS absorber layer, CdS window layer, ZnO, and the ITO transparent conductive oxide. Mo is evaporated by electron beam. CZT is RF sputtered and sulfurized, and CdS is deposited by molecular

beam epitaxy. ZnO and ITO are deposited using an ion assisted deposition (IAD) tool.

2.1.1 *Ion Assisted Deposition*

Ion assisted deposition (IAD) utilizes a plasma generated ion beam that assists a standard electron beam evaporation deposition. This technique allows independent control of both deposition rate and ion energy. IAD allows the ability to grow denser and high stability films [45]. Additionally, since the IAD uses a secondary ion source, the substrate can be cleaned via oxygen plasma before deposition to decrease possible contamination.

2.1.2 *Sputtering*

Sputtering involves bombarding a target material by plasma-generated ions. The atoms from the target are then removed from the bombardment process and condensed onto a substrate as a thin film.

Magnetron sputtering uses magnets to create a magnetic pole at the central axis of the target and one at the ring around the outer edge of the target to trap electrons. These electrons will move in a spiral motion until collision with an argon atom [46]. This will increase ionization efficiency, by increasing ion bombardment of the target, leading to higher deposition rates [47]. Additionally, sputtered films have better film qualities and step coverage than evaporated films due to its higher kinetic energy conditions [46]. Sputtering allows high volume manufacturing, high deposition rates, and high reproducibility [21].

2.1.3 *Molecular Beam Epitaxy*

Molecular beam epitaxy (MBE) was chosen to deposit CdS due to its high purity depositions. Films grown via MBE are deposited approximately one atomic monolayer/second. Because the layer of CdS is very thin, the slow growth rate is not significant. Additionally, MBE allows great control of purity in deposited materials. However, because of the small size of the system, MBE has very low throughput.

2.2 Molybdenum Back Contact

The back contact material for this cell will be molybdenum. Figure 8 compares the thickness of Mo with parameters such as efficiency, FF, V_{oc}, and I_{sc} for a CIGS cell [38]. The Mo thicknesses chosen for this experiment is 200 nm to allow the out-diffusion of Mo into the deposited CZTS film.

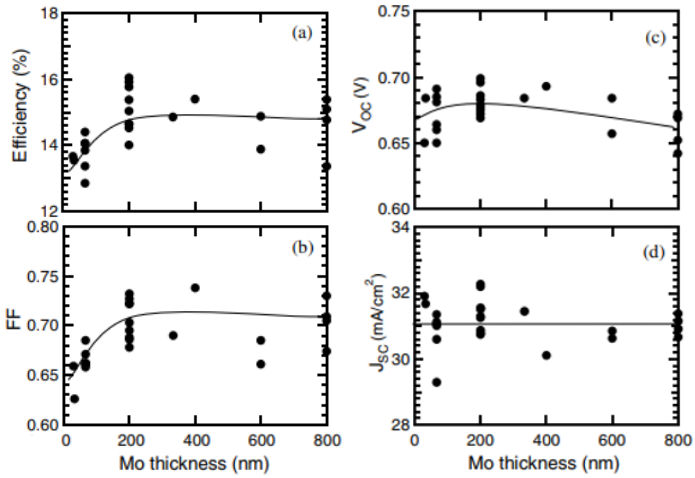

Figure 8 – Efficiency, Fill Factor, V_{OC}, and $J_{S\ C}$ vs Mo Thickness. From [38].

2.3 CZTS Absorber Layer

Depositing CZTS from a single target by sputtering allows for a more uniform composition of the film, stability, smoother surfaces, and high reproducibility [41, 48]. This option of a single $Cu_{49.5}Zn_{27.5}Sn_{23}$ target instead of multiple targets allow for a less expensive process. The sulfur will be added through a sulfurization process with the flow of plasma assisted H_2S. The target composition of the CZTS layer was chosen to be $Cu_{26.53}Zn_{14.75}Sn_{12.31}S_{46.41}$ (atomic percentages) for having smooth surfaces, no undesired secondary phases, and good uniformity[21, 49]. A single target, instead of co-sputtering, was used because single-target sputtered films have no voids present [32]. The voids and low bandgap secondary phases contribute to bulk recombination decreasing FF and V_{OC} significantly. In addition, the absorber/buffer layer interface can introduce lattice misfits and conduction band offset that negatively impacts device performance [21].

It was found that a lower working pressure of 1 mtorr results in a larger grain size, and contributed to higher efficiency [21, 49]. Figure 9 shows the improvement of voltage and current density with lower working pressure. The thickness of sputtered CZTS for the best made solar cells are 1.2 μm [21]. Figure 10 shows thicknesses of the CZTS absorber layer with their respective efficiency. Although, Zhang stated that the optimum CZTS thickness should be 2-3 μm from simulations due to higher light absorption from a thicker layer [21, 50].

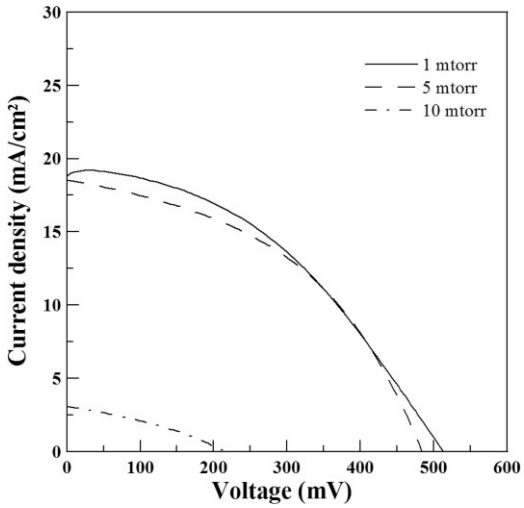

Figure 9 – Voltage vs current density of CZTS solar cells varying pressure. From [49].

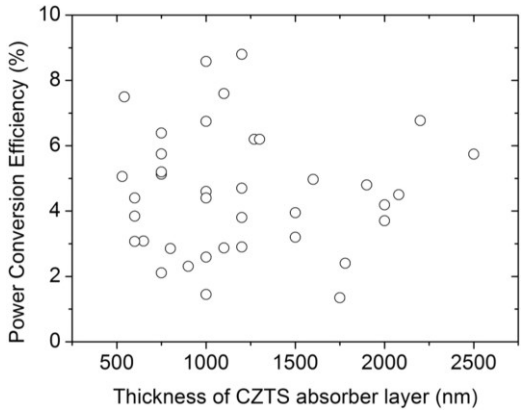

Figure 10 – CZTS thickness vs Efficiency From [21].

For this experiment, the thicknesses of CZT will be sputtered in the range of 1100-1400 nm from a single target. A lower sputtering working pressure contributes to a larger mean free path, allowing for higher film quality [21].

2.4 Thermal Anneal Sulfurization

A post deposition thermal anneal treatment, typically around 500-600 °C, is typically done to form a more uniform and denser grain structure [51]. This allows for fewer

recombination sites for carriers. The annealing process leads to grain growth of CZTS, which causes internal compressive stress relaxation and increased copper content, and triggers a reduction of bandgap in annealed CZTS films [52].

2.5 CdS Window Layer

The window layer is used to create the semiconductor p-n junction along with the absorber layer. This layer needs to have minimal absorption, recombination, and resistive losses to optimize photo-generation. CdS is chosen to be the window layer due to its high bandgap, 2.4eV, and along with its low absorption losses is used to form a junction with the CZTS absorber layer. In order to achieve low recombination rates and minimum absorption, the window layer must be very thin. Simulation results from Courel in Figure 11 show the efficiency of a CZTS solar cell with varying CZTS and CdS widths [13]. The thicknesses of the CdS window layer is chosen according to the simulated results by Courel. This will range from 20-30 nm, for 1.2-1.3 µm of CZTS, to prevent absorption losses.

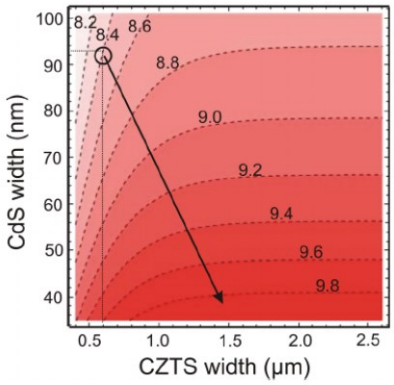

Figure 11 – Contour plot of CdS:CZTS efficiency as a function of their corresponding thicknesses. From [13].

2.6 ZnO High Resistance Transparent Layer

A high resistance transparent (HRT) layer is needed between the CdS and the transparent conductive oxide (TCO) to prevent electrical inhomogeneity through the device from dominating the V_{oc} of the entire device [53]. ZnO is chosen to be the HRT between the CdS and the transparent conductive oxide for this device. This layer is also used for preventing degradation of the device parameters, such as V_{oc} and is necessary when the window layer CdS is very thin [53, 54]. ZnO between the window layer and TCO prevents shunting of paths through the n-type layer, increasing V_{OC}, and R_{SH} by passivation [21, 22]. The thickness of ZnO chosen for this proposed research will range from 10-30 nm.

2.7 ITO Transparent Conductive Oxide

The top contact of the solar cell is made of a transparent material in order to allow photons to interact with the p-n junction. The electrode material is usually a transparent conductive oxide (TCO), providing low resistance electrical contacts and transparency. In order to achieve photon penetration through the oxide, the bandgap of the oxide needs to be greater than that of visible light (1.8-3.1 eV) [55]. Indium tin oxide (ITO) is chosen for being transparent to visible light (>85%) having a bandgap of approximately 4 eV. Additionally, ITO exhibits strong adhesion to many substrates and high electrical conductivity of 10^{-5} Ω-cm [56]. IAD of ITO was found to produce near constant high transmission value (>90%) for wavelengths from 600-933 nm along with a R_{sheet} of 23.13 Ω/□ [57].

III EXPERIMENTAL PROCEDURE

The fabrication process of the CZTS PV device includes an e-beam deposition of the Mo back contact, CZT deposition, sulfurization of CZT, CdS deposition, ZnO passivation layer, and ITO as the top contact. Polished, 500 μm thick, soda lime glass (SLG) (University Wafer) were used as the substrate.

3.1 Cleaning

The SLG wafers are cleaned with acetone, methanol, and isopropyl alcohol using a sonicator bath for 3 minutes each. They are then immediately rinsed with copious amounts of deionized (DI) water to remove any organic residues. Nitrogen is then used to thoroughly blow dry the wafers.

3.2 Molybdenum Deposition

The IAD system used to deposit molybdenum is a Leybold (Pf˙affikon, Switzerland) APS 1104 (Figure 12). The molybdenum source material is 4N purity in 1/8" diameter by 1/8" long pellets from Kurt J Lesker.

After cleaning the substrate, the samples are then attached to the hemispherical sample holder, via Kapton tape, and is rotated. The molybdenum is then evaporated at a rate of 0.05 nm/s until a thickness of 200 nm is measured with the quartz crystal deposition rate monitor. The thickness can be further confirmed by using a scanning electron microscope (SEM) to analyze the cross section of the substrate.

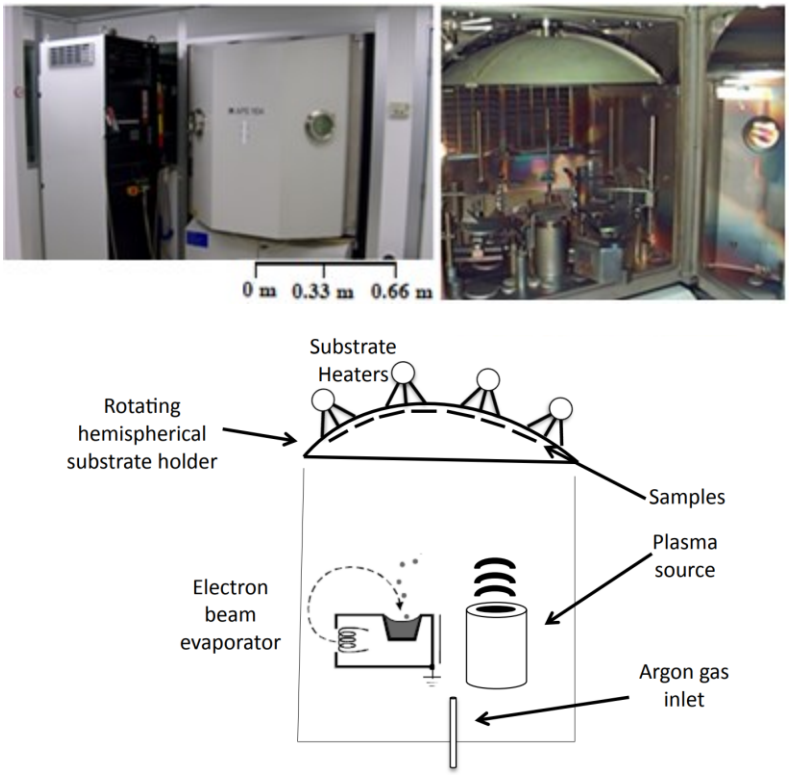

Figure 12 – (Top left) Exterior of Leybold IAD system. (Top right) Interior view of Leybold IAD system. (Bottom) Schematic of IAD components. The system has a rotatable substrate holder that can be heated, an electron beam evaporator, inlets for various gases, and a plasma source. From [57].

3.3 Sputtering of CZT

The system used to deposit CZT is an Angstrom Engineering EVOVAC deposition system (Kitchener, ON) shown in Figure 13. The CZT target has the composition $Cu_{49.5}Zn_{27.5}Sn_{23}$ (At%) fabricated by Plasmaterials (Livermore, CA).

After the deposition of the back contact, the sample is attached to a rotatable sample holder via screws and is heated to 150 °C. The chamber is pumped down until the pressure is approximately 2E-7 torr. CZT is sputtered onto the sample at a rate of 0.3 ± 0.1 Å/s, with 100 W of RF power held at a pressure of 4.2 mtorr, until the quartz crystal measures 1300 nm.

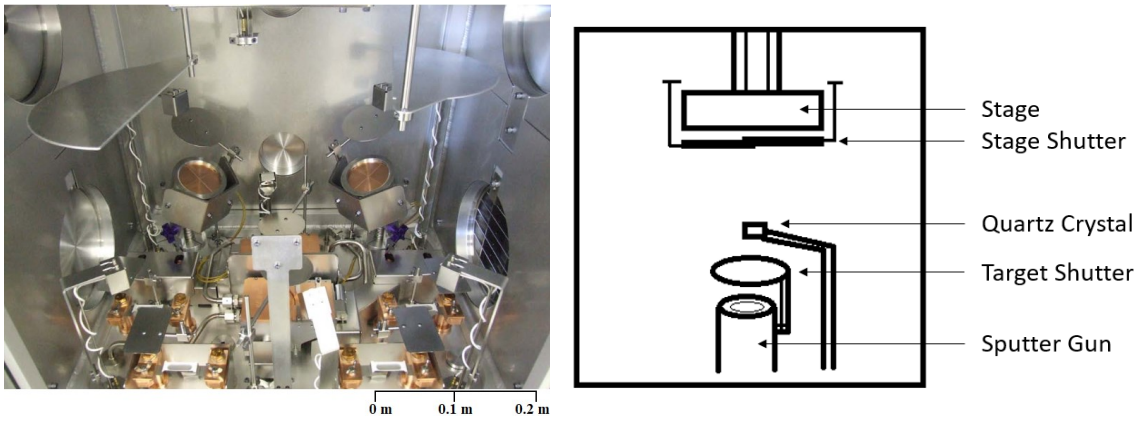

Figure 13 – System used to sputter CZT. (Left) Interior view of Angstrom EVOVAC system. (Right) Diagram of system used for sputtering. The system is capable of sputtering (DC and RF), e-beam evaporation, and thermal evaporation.

3.4 Sulfurization and CdS

An MBE tool was used for sulfurization. This tool is capable of having up to eight molecular sources allowing for sequential depositions. The base pressure used for this system can achieve a pressure on the order of 10^{-9} torr. There are shutters that control the flow of sources during each deposition. A schematic of the MBE tool is shown in Figure 14. The sample is mounted on a rotating assembly with an ion gauge mounted on the opposite side of the sample. Additionally, there is liquid nitrogen cryo-shroud, which allows lower chamber pressure by freezing out atmospheric species. In this work, a direct plasma source used for H_2S plasma sulfurization, and epitaxial growth for the CdS window layer.

Once the sample is mounted to the rotatable holder, the substrate is heated to 510 °C using a Veeco VA2-SSH substrate heater. Next, an 86% flow of H_2S is introduced to the chamber using a MKS Instruments type 1459C mass flow controller (rated for 50 sccm of N_2).

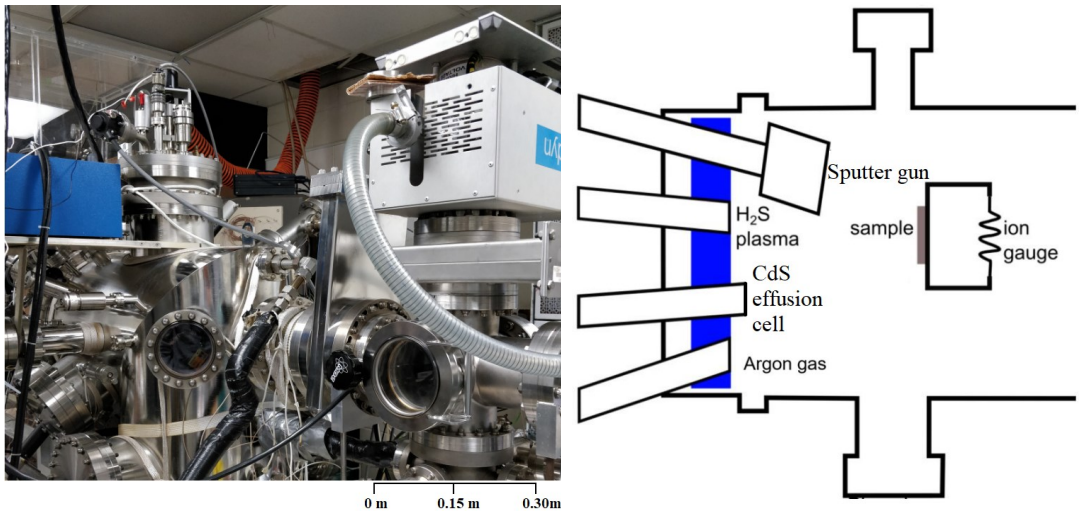

Figure 14 – MBE system used to sulfurize CZT and deposit CdS. (Left) MBE system. (Right) Diagram of the MBE system used for sulfurization of CZT and CdS deposition. From [58].

The stage heater is then cooled down to 200 °C. The deposition rate of the CdS n-type window layer is found by running flux tests at different temperatures. The ionization gauge is turned on once the temperature of the CdS effusion cell is stabilized and the pressure is noted. The CdS effusion cell shutter is then open briefly for 2-3 seconds and the pressure is noted. The beam equivalent pressure (BEP) is found by computing the difference between the pressure when the shutter to the CdS effusion cell is open and closed. A typical BEP testing process is shown in Figure 15.

Once the desired BEP is reached, the shutter to the CdS effusion cell is open for a certain amount of time. The thickness is then measured using a profilometer and the deposition rate at the BEP can be determined.

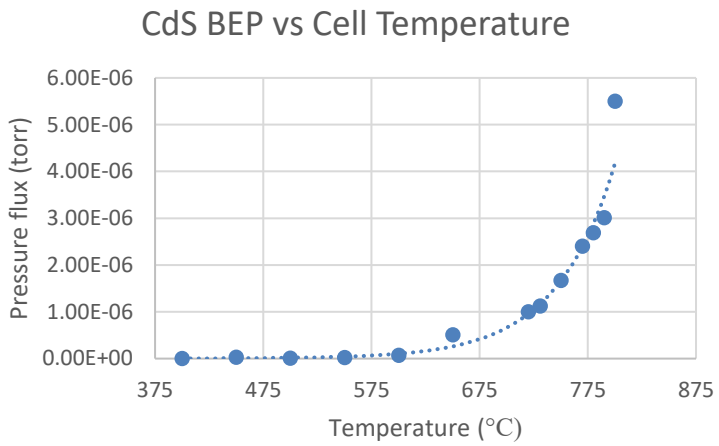

Figure 15 – CdS BEP vs effusion cell temperature from beam flux testing.

3.5 ZnO and ITO Deposition

After the CdS deposition, the sample is taped down onto the stage of Leybold (Pf˙affikon, Switzerland) APS 1104 IAD system for ZnO and ITO deposition sequentially. The ZnO source material is 4N purity in 8-12 mm tablets and the ITO source material is 4N purity in 1/8" diameter by 1/4" long pieces, both from Kurt J. Lesker.

The stage rotation is turned as well as the plasma source while the electron beam gun is ramping up to desired ZnO deposition parameters shown in Table 1. During the deposition, 9 sccm of O_2 is flowing and the rate is kept constant at 0.01 nm/s until a thickness of 20 nm is measured with the quartz crystal deposition monitor. The tooling factor is adjusted to the previous thickness to achieve the correct thickness.

Once the nominal thickness of ZnO is achieved, the stage is heated up to 250 °C. Then, the plasma source and electron beam gun ramp up to the desired ITO deposition parameters shown in Table 1. During the deposition, 15 sccm of O_2 is flowing and material is deposited for 150 nm, where the rate is 0.01 nm/s for 5 nm and then 0.1 nm/s for 145 nm.

The deposition ends once the quartz crystal monitor measures an ITO thickness of 150 nm, where the tooling factor is adjusted to the previous thickness.

Table 1 – Plasma and electron beam gun parameters for ZnO and ITO deposition. These parameters were adjusted for the APS 1104 IAD system.

Material	E-beam Emission Current (mA)	Plasma Discharge Current (A)	Plasma Bias Voltage (V)	Plasma Discharge Voltage (V)	Plasma O_2 Gas Flow (sccm)
ZnO	21.3	50	80	70	12
ITO	35.5	50	85	65	10

IV RESULTS

4.1 Molybdenum Deposition

Two different electron beam evaporators were tested with depositing molybdenum. The first tool tested with molybdenum deposition was a Denton Explorer E-Beam evaporator (Beijing, China). The R_{sheet} of the deposited Mo using this tool was too high for the desired thickness of 200 nm. However, the Leybold (Pf˙affikon, Switzerland) APS 1104 deposition tool resulted in more conductive films for the same thicknesses. The R_{sheet} of the Mo deposited by the Leybold was 15.31 ± 0.2 Ω/□ for approximately 200 nm. This may be due to a lower processing pressure the APS 1104 is able to achieve. The Leybold recipe will be used with all of the subsequent depositions. The thickness of molybdenum compared to R_{sheet} is shown in Figure 16 between the two deposition tools.

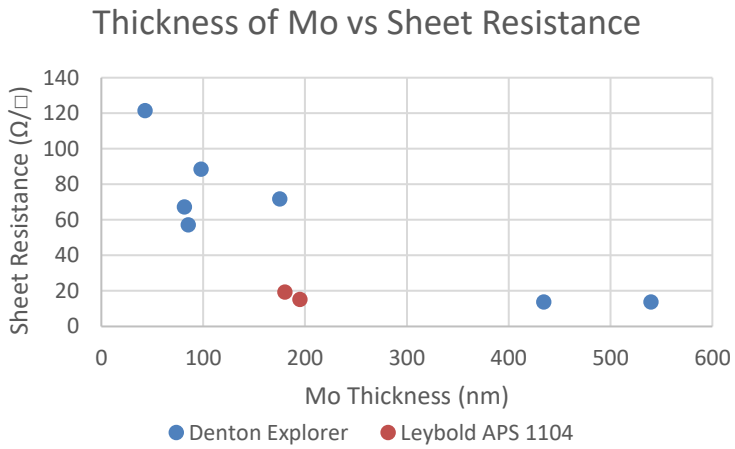

Figure 16 – Sheet resistance of molybdenum vs thickness. Molybdenum was deposited via Denton Explorer E-Beam evaporator and the Leybold APS 1104. The film deposited by the APS 1104 show to have greater conductive properties than the Denton Explorer.

The deposited film is evaluated using a Hitachi SU8030 SEM (Chiyoda, Tokyo, Japan) as shown in the micrograph in Figure 17. The thickness of the deposited Mo is approximately 196 nm. Additionally, the film is shown to be very uniform in thickness.

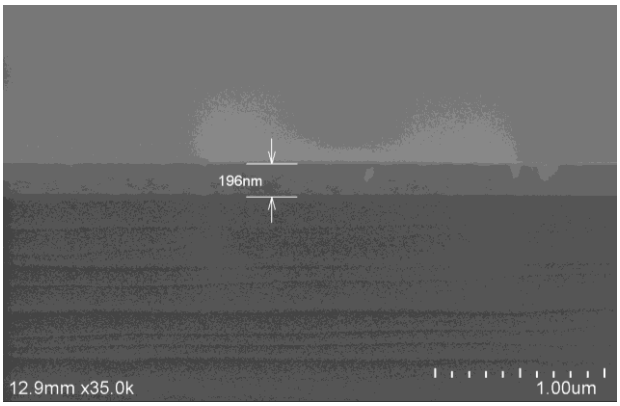

Figure 17 – SEM micrograph of Mo deposited using the Leybold APS 1104 electron beam gun.

4.2 CZT Deposition

A series of 12 different depositions were done to create the desired process recipe. In order to achieve a clean, smooth, CZT deposition, it was crucial to have a substrate temperature approximately 150 °C and a lower working pressure. The targeted thickness for CZT was 1300 nm. Due to limitations on the tool to maintain a low pressure, a constant 1 mtorr working pressure was not achievable. Instead, the lowest obtainable constant working pressure was 4.2 mtorr. The parameters and results of the CZT depositions are shown in Table 2.

Table 2 – Table of parameters and of CZT sputter deposition. The power was automatically adjusted to maintain the deposition rate.

Sample Name	Deposition Rate (Å/s)	Thickness (nm)	Working Pressure (mtorr)
CZT_1	0.3	1000-1200	4.2
CZT_2	0.2	1200-1400	4.2

The sample CZT_1 was sputtered continuously for approximately 14 hours, at 145 W RF power, in order to achieve a thickness of 1.3 μm. The deposition rate at this power resulted in approximately 0.4 nm/s. The prolonged high temperature exposure of the target while sputtering resulted in the backing plate of the target to separate. Due to the nature of the material being rough, the measured thickness of the CZT for this deposition was approximately 1.1 ± 0.1 μm.

Due to the backing plate separating from the CZT target from the long deposition time, the next process was cycled between depositions and cooling in order to prevent the backing plate from separating from the CZT target. Additionally, the RF sputter power was lowered to 100 W in order to prevent the indium solder from melting. The deposition was performed at 150 nm intervals with a post-deposition cooling phase of 1 hour. The deposition rate of 0.2 ± 0.05 nm/s was achieved with an RF power of 100 W. During the cooling phase, the stage heater was kept constant for 150 °C.

CZT_2 was shown to have a denser grain structure as well as a smoother surface than CZT_1 (Figure 18). Having a higher RF power, higher deposition rate and a continuous deposition may be the reason for inconsistent grain sizes as seen in CZT_1.

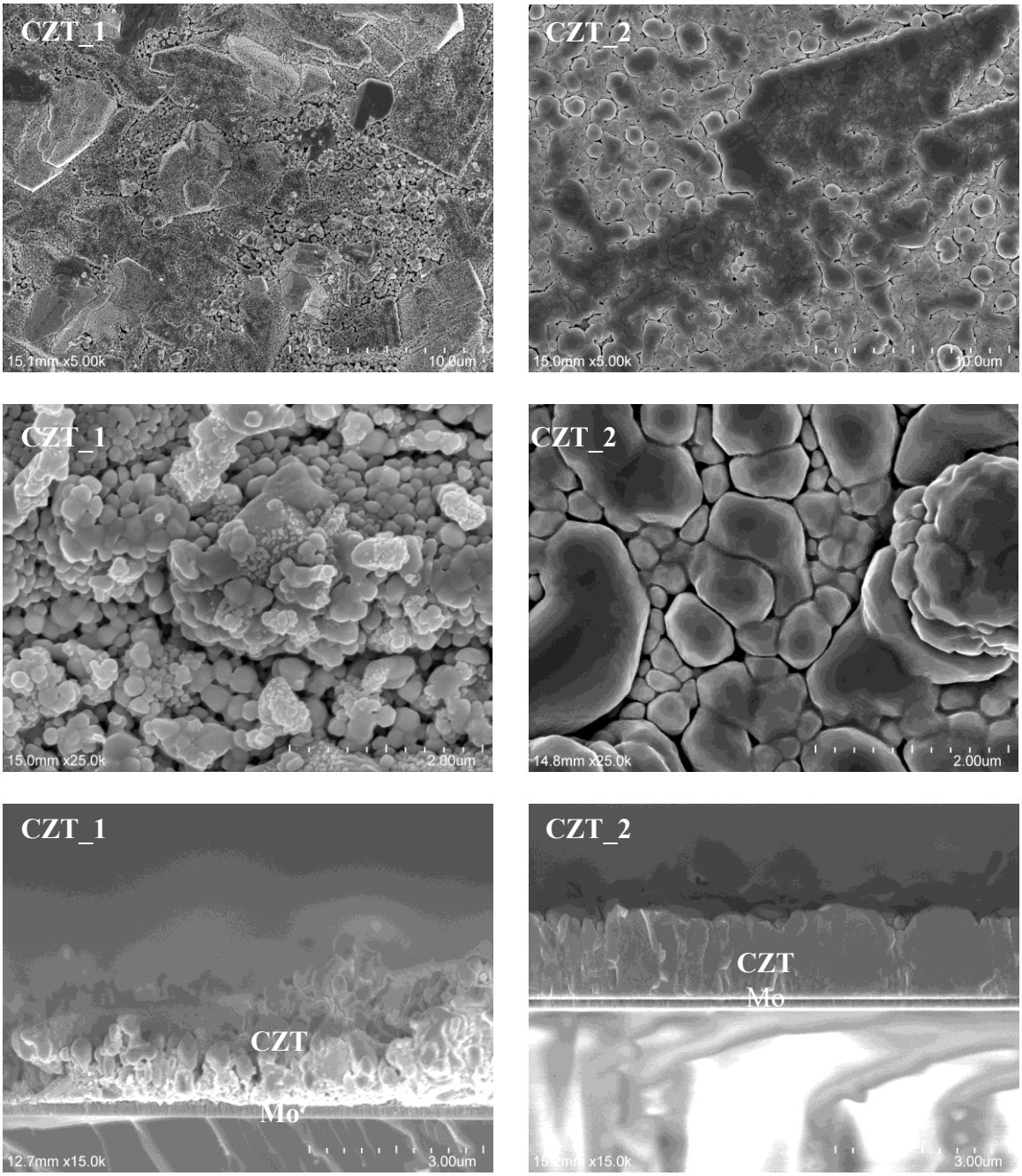

Figure 18 – SEM micrographs of CZT samples. (Left) SEM micrograph of CZT_1 and (right) CZT_2. Both are deposited by RF sputter. (Bottom Left) Cross section of CZT_1. (Bottom Right) Cross section of CZT_2. The CZT microstructure exhibits greater smoothness and uniformity in CZT_2 than CZT_1. The cross sections of both show that CZT_2 has a denser grain structure than CZT_1. Additionally, the grains in CZT_1 have inconsistent sizes resulting in more voids throughout the material.

EDS was used to determine the compositions of the sputtered CZT samples shown in Table 3. The composition of copper, in CZT_2, is shown to have increased when the deposition was at a lower power and rate. For CZT_1, the copper and zinc composition decreased while the tin has increased.

Table 3 – Comparison between the composition of deposited CZT and the CZT sputter target.

	Cu (at%)	Zn (at%)	Sn (at%)
CZT_1	43.1	20.6	36.3
CZT_2	58.2	23.1	18.7
CZT Target	49.5	27.5	23.0

4.3 CZTS Sulfurization

Many experiments have been performed to attempt to obtain the CZTS stoichiometry. The process parameters that were changed include the substrate heater temperature, time of sulfurization, the amount of H_2S flow, and process pressure. These process parameters and CZTS composition results from EDS are shown in Table 4.

A comparison of the compositions of copper, zinc, tin, and sulfur in the sulfurized CZTS layer is shown in Figure 19. Many of the sulfurization processes resulted in low zinc, or low sulfur. When a deficit of copper was present, tin showed to be dominant.

Table 4 – Sulfurization process parameters and its respective EDS composition of CZTS. The temperature, time, flow of H_2S, and pressure are the parameters changed. A soft temperature anneal of 350 °C was added to some of the later runs.

	Substrate Temp. (°C)	Time (min)	H2S Flow (sccm)	Process Pressure (torr)	Cu (at%)	Zn (at%)	Sn (at%)	S (at%)	CZT layer
Sulf_1	575	30	25	3×10^{-5}	19.2	16.7	52.9	11.3	CZT_10
Sulf_2	510	15	12.5	3×10^{-5}	25.3	14.3	52.8	7.6	CZT_10
Sulf_3	510	30	12.5	3×10^{-5}	20.6	14.2	47.7	17.5	CZT_10
Sulf_4	510	60	12.5	3×10^{-5}	21.1	6.6	47.7	24.6	CZT_10
Sulf_5	510	90	12.5	3×10^{-5}	18.5	2.8	46.3	32.4	CZT_10
Sulf_6	510	60	43	3×10^{-5}	55.5	0.5	9.5	34.5	CZT_10
Sulf_7	1) 350	1) 30 2) 30	43	3×10^{-5}	45.7	22.3	18.2	13.8	CZT_12
Sulf_8	1) 350	1) 30 2) 60	43	3×10^{-5}	27.5	36	11.8	24.7	CZT_12
Sulf_9	1) 350	1) 60 2) 30	43	3×10^{-5}	37.2	30.6	15.4	16.7	CZT_12
Sulf_10	350	60	43	3×10^{-5}	47.5	26.2	18.8	7.5	CZT_12
Sulf_11	510	60	12.5	3×10^{-3}	72.2	0	25.4	2.5	CZT_12

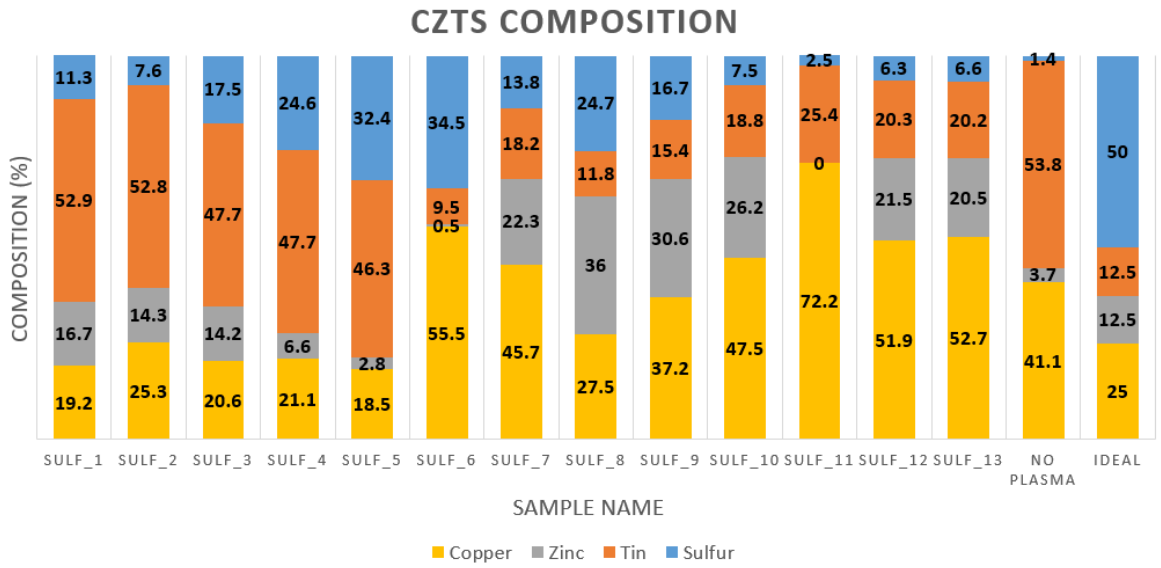

Figure 19 – CZTS composition of different sulfurization parameters.

4.3.1 *Temperature*

A high temperature sulfur anneal of 575 °C resulted in cracks on the surface of the CZTS layer (Figure 20) as shown in the sample of Sulf_1. These cracks seem to be rich in copper and sulfur. The avoidance of these defects is crucial for greater electrical performance.

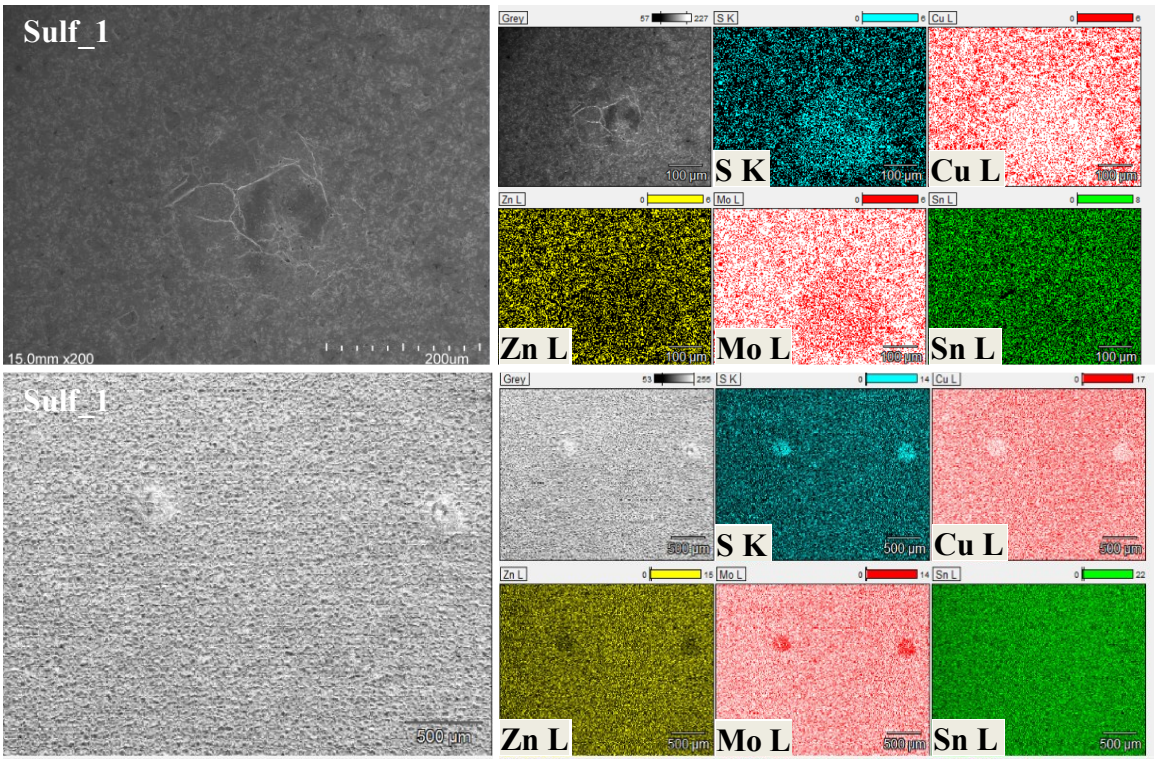

Figure 20 – Energy-dispersive X-ray spectroscopy (EDS) focused on the crack formations on the surface of the CZTS layer. These cracks are shown to be copper and sulfur dense. (Top) Higher magnification of a surface crack deformation. (Bottom) Lower magnification of two different crack formations.

A lower temperature hard anneal of 510 °C was found to prevent the formation of these defects. However, if the sulfurization time is too long, 30-90 min, bumps or surface extrusions form. Additionally, if the sulfurization time was short, 15 min, the surface deformities are non-existent. EDS results in Figure 21 show that the composition of the extrusions formed utilizing a lower temperature are mostly copper and tin.

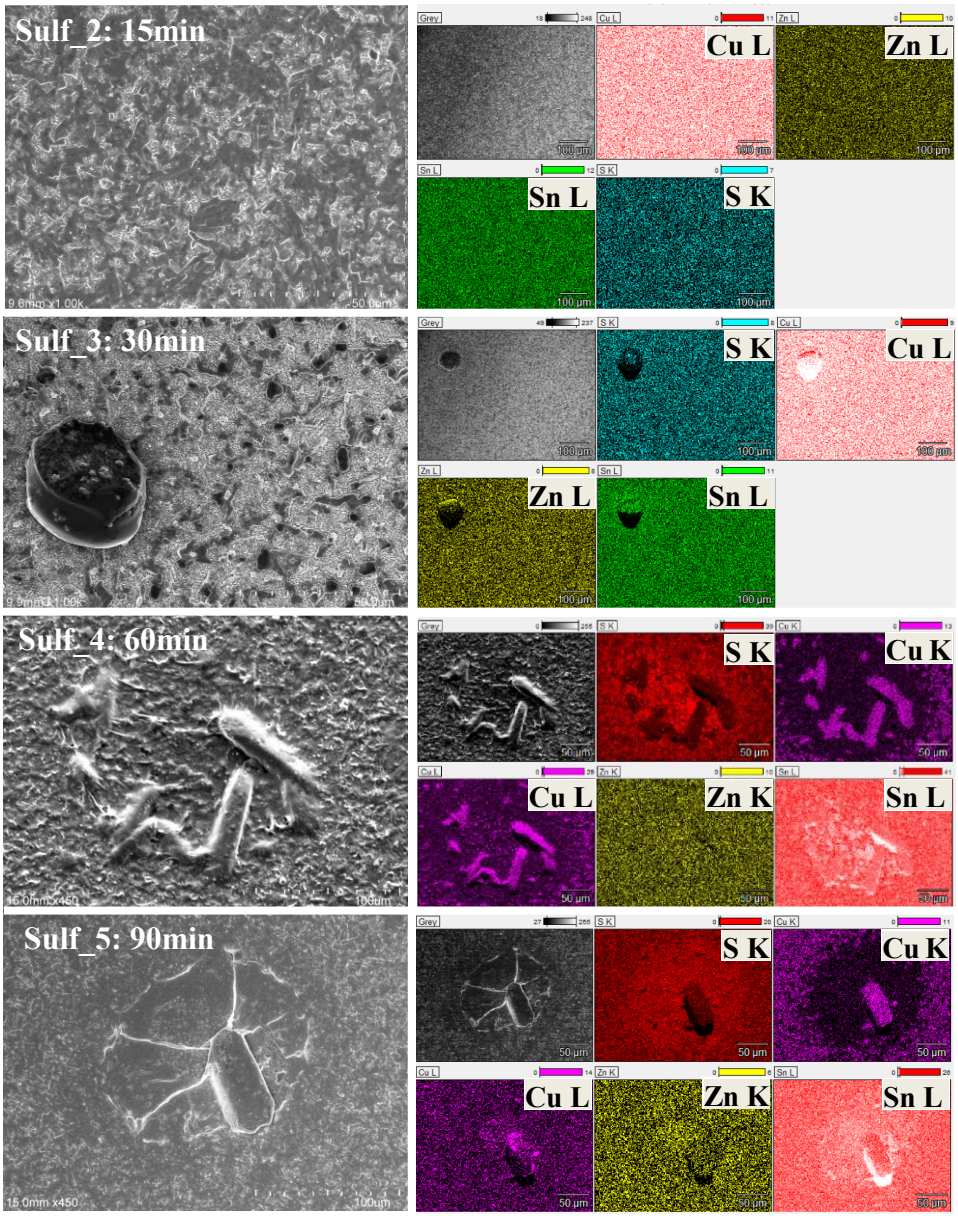

Figure 21 – SEM micrograph of sulfurization processes done at 510 °C. With the annealing times of 15 min for Sulf_2, 30 min for Sulf_3, 60 min for Sulf_4, and 90 min for Sulf_5. Surface defects occur at longer sulfurization times.

As for the most of the surface area of these samples, the amount of zinc decreases drastically down to 2-6% when the sulfurization time was long. The increased sulfur content at these longer times is expected. Additionally, all of these CZTS samples are tin-rich and sulfur-poor. Given the composition of CZTS in these samples (Table 4), the concentration of sulfur and tin needs to be adjusted to achieve the desired CZTS composition.

4.3.2 *Impact of plasma*

Without plasma, the sulfur and zinc content was almost non-existent. During this run, a sample was sulfurized at 510 °C for 30 min with only 12.5 sccm of H_2S flowing. Similar to the plasma-assisted sulfurization discussed previously, surface extrusions are present after the process. However, EDS analysis show that these defects are sulfur-rich, tin-poor and copper-poor (Figure 22). The plasma is crucial when working with H_2S sulfurization to increase the sulfur content in CZTS and to maintain copper and tin. For all the sulfurization processes, the power of the plasma was kept constant at 235 W.

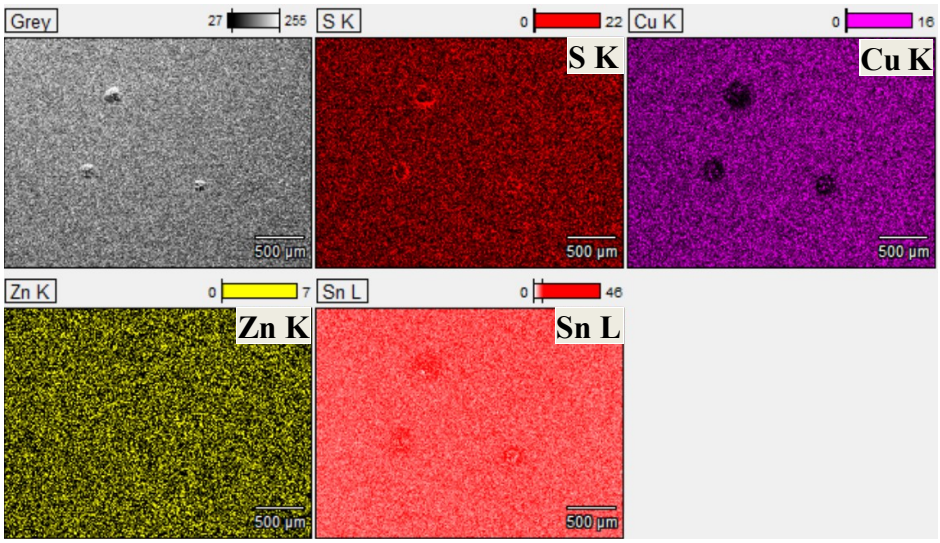

Figure 22 – EDS analysis on CZTS without the use of plasma.

4.3.3 *Flow Rate*

When the gas flow was increased to approximately 43 sccm, the extrusions ceased to form. Additionally, the sulfurization process at 510C for 1 hour increased sulfur content by approximately 10% between Sulf_4 (12.5 sccm H_2S) and Sulf_6 (43 sccm of H_2S). The increased flow rate increased the amount of copper in the CZTS layer. However, the

amount of zinc during this hour sulfurization decreased significantly than that of a lower flow rate. It is clear that long sulfurization times with or without plasma results in critical zinc degradation (as shown in samples Sulf_4, Sulf_5, Sulf_6). Another step is needed to increase the sulfur content without sacrificing too much zinc.

4.3.4 *Addition of Soft Anneal Step*

The introduction of a soft annealing sulfurization step before a hard anneal resulted in a more uniform grain structure as shown in Figure 23. The soft anneal temperature was chosen according to the melting points of copper, zinc, and tin (1085 °C, 419.5 °C, 231.9 °C respectively). Because the samples with the hard anneal alone resulted in an excess concentration of tin, 350 °C was chosen above the melting point of tin but below copper and zinc. EDS analysis of samples with the addition of the soft annealing process resulted in less zinc degradation Figure 24.

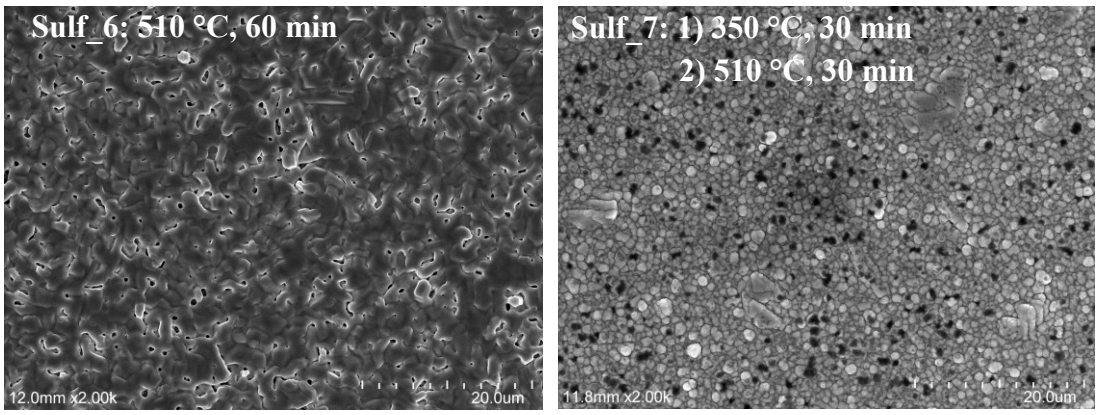

Figure 23 – SEM micrographs of CZTS with and without a soft anneal sulfurization. (Left) Sulf_6: Sulfurization process with only a hard anneal step at 510 °C for 60 min. (Right) Sulf_7: Adding a soft anneal step at 350 °C for 30 min, followed by a hard anneal step at 510 °C for 30 min. The addition of a soft anneal step resulted in greater uniformity in grain sizes than the hard anneal alone.

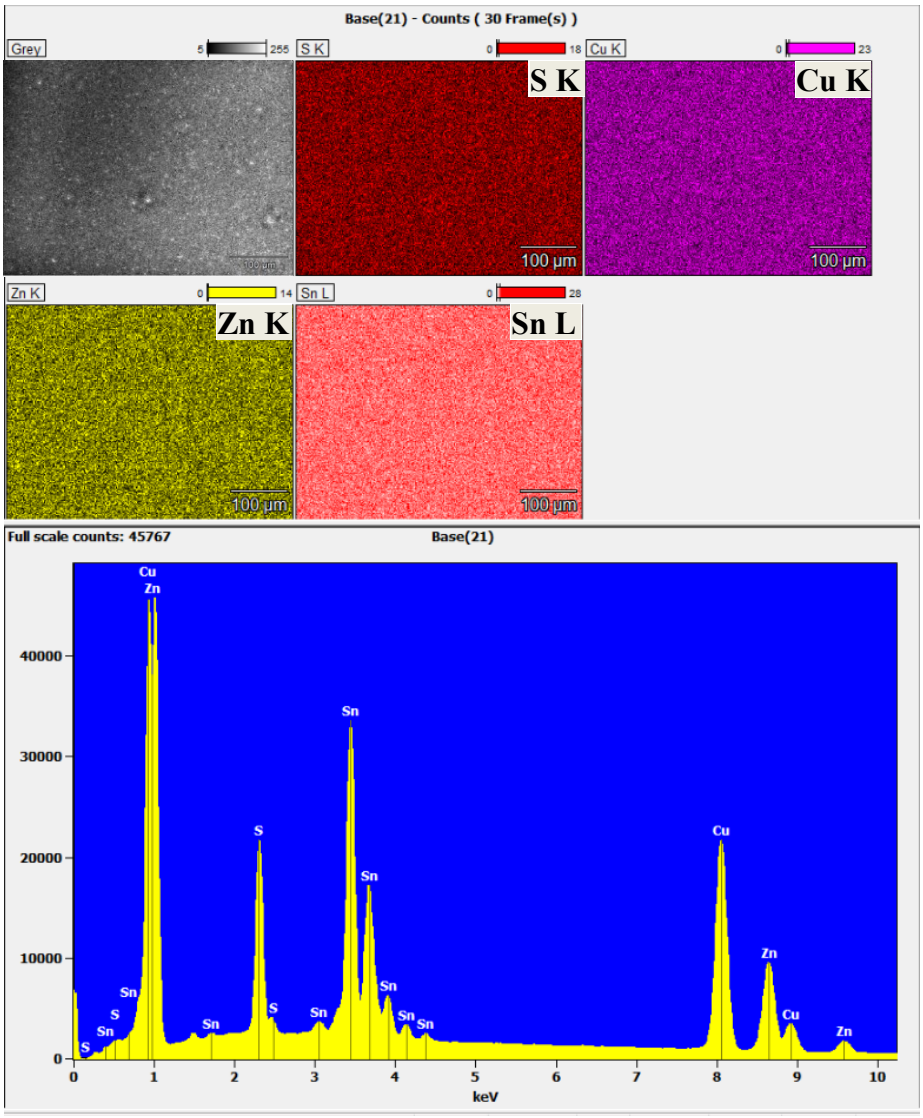

Figure 24 – EDS analysis of a CZTS sulfurization sample, Sulf_7, with the addition of a soft anneal step at 350 °C prior to the hard anneal step of 510 °C.

The CZTS ratio of samples with a soft anneal sulfurization step showed a good CZT ratio, but is lacking in sulfur. Unfortunately, the soft annealing process may have resulted in bad adhesion of CZTS on Mo. After the sulfurization process, some of the CZTS film became brittle and exfoliates from the Mo (Figure 25).

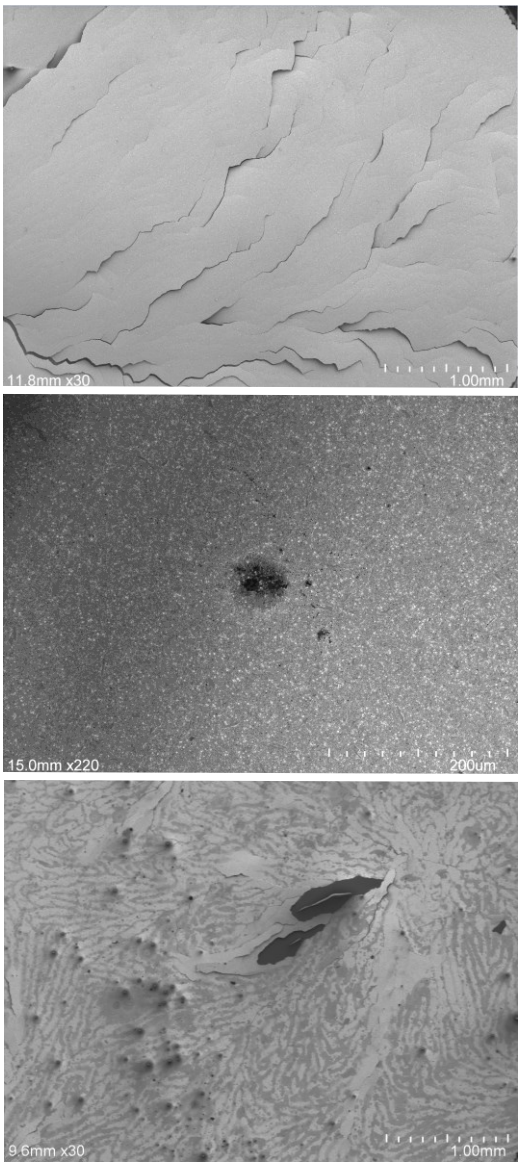

Figure 25 – Surface defects exhibited by adding a soft anneal process. (Top left) Sulf_7: soft anneal step at 350 °C for 30 min prior to the hard anneal step of 510 °C for 30 min. (Top right) Sulf_9: soft anneal step at 350 °C for 60 min prior to the hard anneal step of 510 °C for 30 min. (Bottom) Sulf_10: 60 min of sulfurization at 350 °C.

However, the SEM micrograph cross section of the CZTS layer in Figure 26 showed that the CZTS had good adhesion to Mo for the samples with a soft anneal step. The source of the brittle CZTS layer remains uncertain. Additionally, the cross-section shows that a higher-pressure sulfurization process results in a grainier, less uniform structure (Figure 26 botttom).

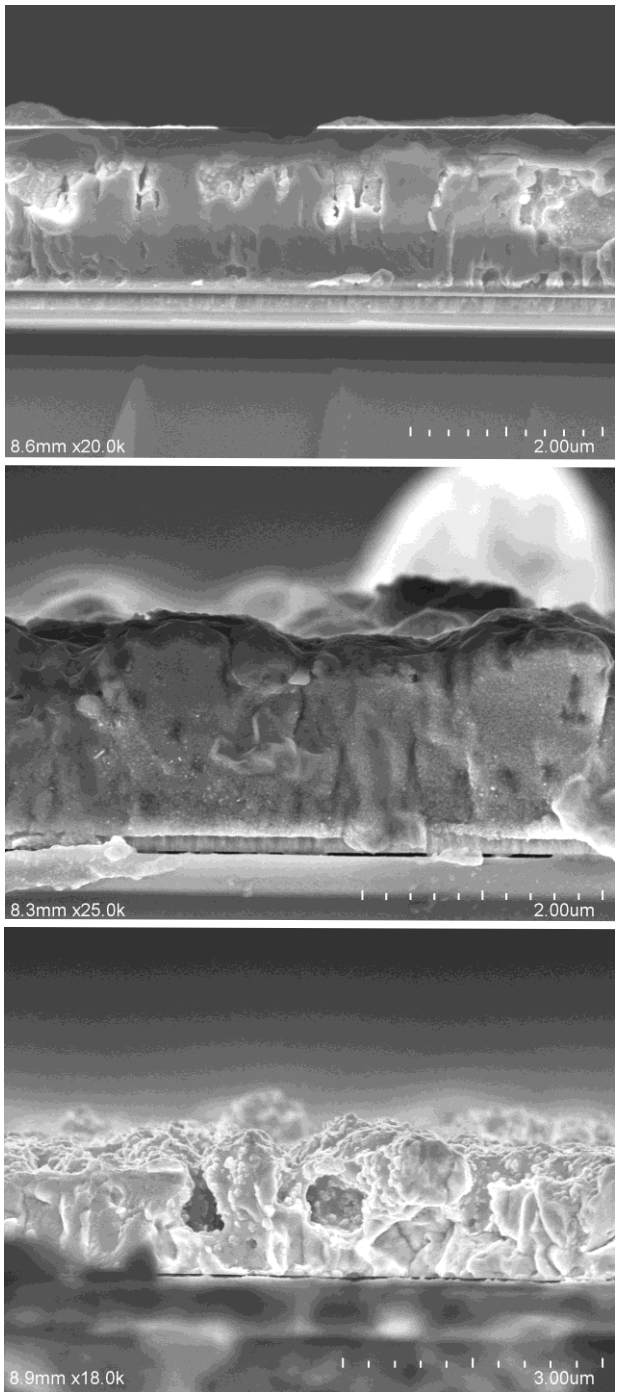

Figure 26 – SEM micrograph of the cross section of sulfurized CZT. (Top) Sulf_7: Soft anneal step at 350 °C for 30 min prior to the hard anneal step of 510 °C for 30 min. (Middle) Sulf_9: soft anneal step at 350 °C for 60 min prior to the hard anneal step of 510 °C for 30 min. (Bottom) Sulf_11: Soft anneal at 350 °C for 60 min.

4.3.5 *Higher Pressure Sulfurization*

The process pressure was increased by two orders of magnitude to attempt to increase the sulfur content in the CZTS layer. The turbo pump was not used in this process due to possible damage from higher pressures. Instead, a Danielson Tribodyn 120XR (Lisle, Illinois) dry pump was used pump down the chamber. A process pressure of approximately 3 x 10^3 torr was achieved.

Using the higher process pressure, Sulf _11 was sulfurized at 510 °C for 60 min with a H2S flow rate of 12.5 sccm. This process resulted in no flaking of the surface. However, EDS results show that there is no zinc present and only 2.5% atomic percentage of sulfur (Figure 27).

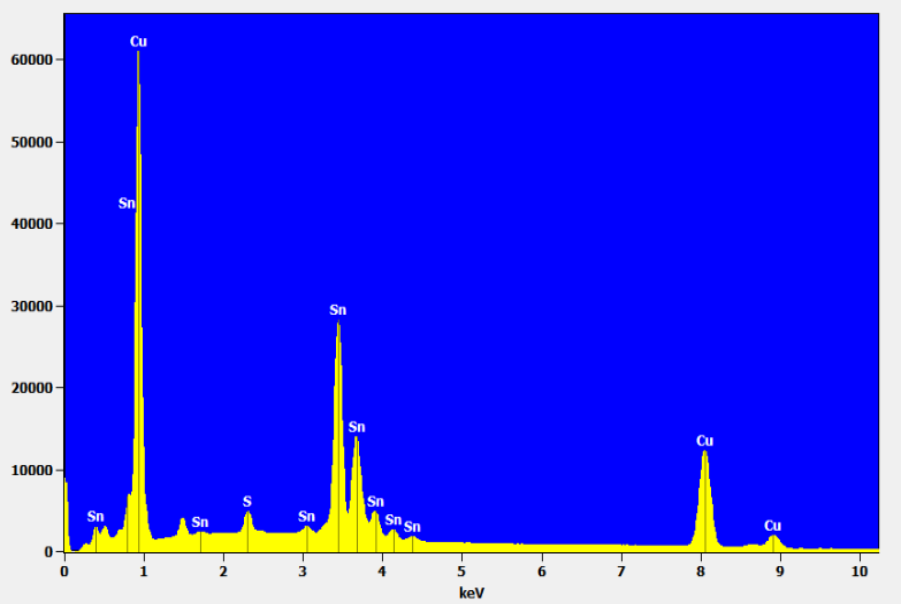

Figure 27 – EDS mapping of Sulf_11 sample. 510 °C for 60 min with a H2S flow rate of 12.5 sccm at a process pressure of 3 x 10^3 torr.

Sulf_12 was done with a soft anneal at 350°C followed by a 510 °C hard anneal for 30 min each at 43 sccm (Figure 28 Top). There were large surface cracks on the CZTS after this deposition Additionally, EDS shows that there was no zinc in the structure.

It was suspected that the high flow rate of H_2S resulted in large surface fissures at high pressures. Another sulfurization process, Sulf_13, was tested using the same soft and hard anneal at 510C, but with different flow rates of H_2S. The soft anneal sulfurization was done with a H_2S flow of 12 sccm while the hard anneal was with a flow of 43 sccm. EDS analysis shows that a lower flow rate of H_2S during the soft anneal process at high pressures prevent zinc degradation that is seen in Sulf_11. However, the surface fissures are still present in this sample (Figure 28 bottom). It was concluded that the higher pressure sulfurization caused the CZTS film to form fissures.

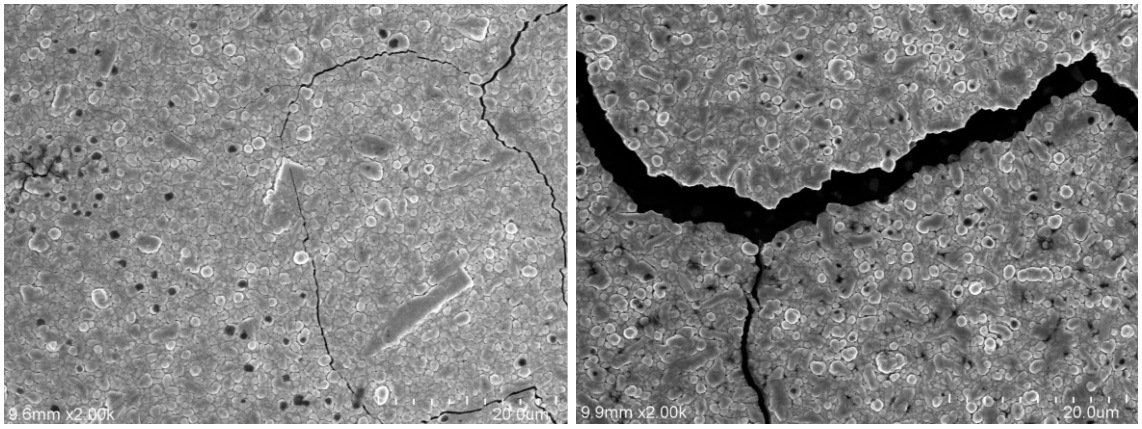

Figure 28 – SEM micrographs showing the formation of surface fissures at higher pressures. (Top) Sulf_12: Sulfurization process with a soft anneal at 350 °C followed by a hard anneal at 510 °C for 30 min each with a H_2S flow rate of 43 sccm. (Bottom) Sulf_13: Sulfurization process with a soft anneal at 350 °C, followed by a hard anneal at 510 °C for 30 min with an H_2S flow rate of 12.5 sccm and 43 sccm respectively.

4.4 CdS Deposition

CdS/SLG samples were created. By using a Tencor P15 profilometer (Milpitas, CA), the deposition rate was determined to be 0.42 nm/s when the BEP is 3.00 x 10^{-6} torr. The temperature required to achieve the given BEP changes after every deposition. The stage heater is then set to 200 °C. Once the BEP is reached, the shutter to the CdS effusion cell is open and is open for approximately 47 seconds in order to have a thickness of 20 nm.

The deposition rate is dependent on the beam equivalent pressure and temperature of the CdS effusion cell. In order to have an accurate deposition rate, the temperature of the cell adjusted to achieve the desired BEP, 3.0 x 10^{-6} torr. Figure 29 shows the temperature of the effusion cell to maintain a deposition rate of 0.42 nm/s.

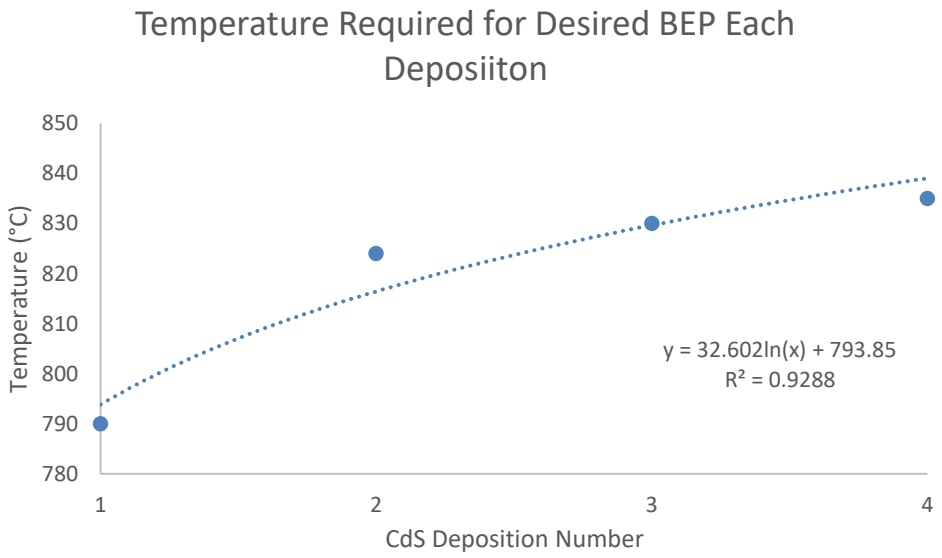

Figure 29 – Temperature required each run to maintain the same BEP of 3.0 x 10^{-6} torr.

4.5 ZnO Deposition

ZnO/SLG samples were created. The transmittance spectrum was obtained using a Cary 5000 UV-Vis-NIR Spectrophotometer (Santa Clara, CA) (Figure 30). The sample, IAD_ZnO_2 having a thickness of 15 nm and 9 sccm flow of oxygen, is shown to have >90% transmittance for all of visible light. Table 5 shows the ZnO deposition parameters.

Figure 30 – Transmittance spectrum of ZnO.

Table 5 – ZnO depositions parameters and the resistivity of deposited films.

	Sample	Thickness (nm)	Resistivity (Ω-cm) * 10^{-4}	O_2 Flow (sccm)
	IAD_ZnO_2_1	15	>1 MΩ	9
	IAD_ZnO_3_1	50	>1 MΩ	9

Unfortunately, the 4-point probe technique used is only able to measure conductive samples and is limited to 1 MΩ/□. This was unable to measure the R_{sheet} for the deposited ZnO. This means that the R_{sheet} of the deposited film is at least 1 MΩ/□.

4.6 ITO Deposition

The R_{sheet} of the ITO films was measured using a 4-point probe technique using a Signatone (Gilroy, CA) #S-302-4 probe station with an #SP4-40085TFS SP4 probe tip connected to a Keithley (Cleveland, OH) 2410 1100 V SourceMeter. The ITO deposited was approximately 150 nm. The R_{sheet} and resistivity of the most recent samples are shown in Table 6 with varying oxygen flow. The increase in oxygen flow during the ITO deposition was shown to increase the R_{sheet} of the film.

Table 6 – Sheet resistance and Resistivity of ITO samples with change in oxygen flow during the process

	Sample	Sheet Resistance (Ω/□)	Resistivity (Ω-cm) * 10^{-4}	O_2 Flow (sccm)
	IAD_ITO_12	25.1526	3.77289	9
	IAD_ITO_13	29.86588	4.479882	15

The transmittance spectrum was obtained using a Cary 5000 UV-Vis-NIR (Santa Clara, CA) spectrophotometer (Figure 31). Most of the visible light spectrum wavelengths are shown to be above 80% transmittance. The transmittance for both the samples from 450 nm to 800 nm exhibit above 90% transmittance. IAD_ITO_13 is has a slightly greater transmittance spectrum than IAD_ITO_12. This is expected due to greater resistivity of the film.

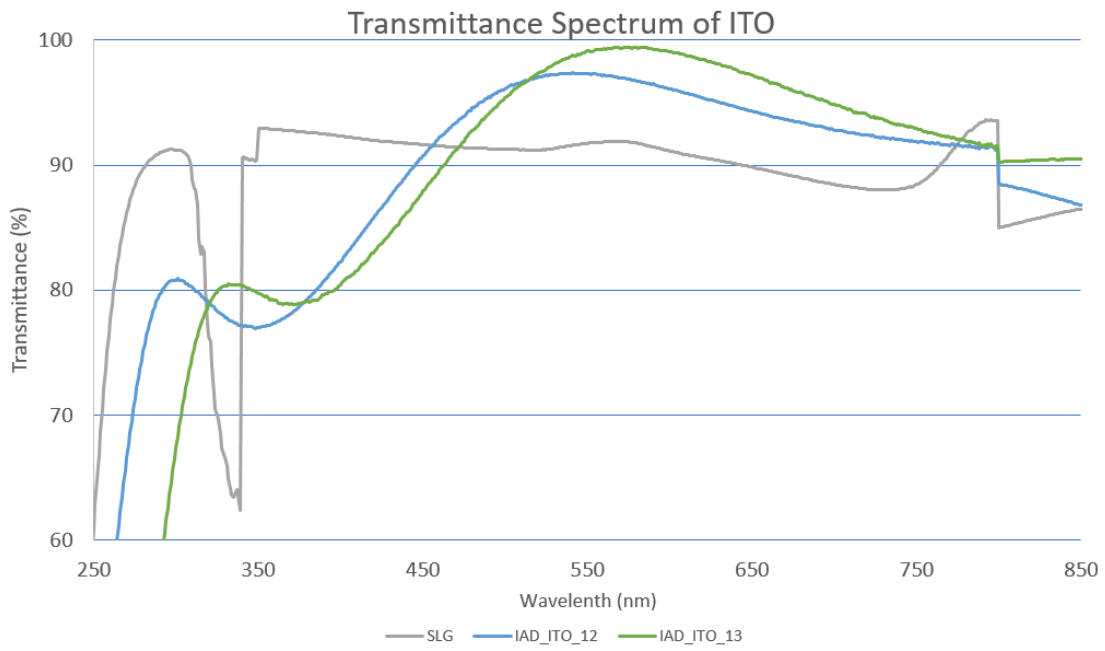

Figure 31 – Transmittance spectrum of ITO samples compared to soda lime glass as the baseline.

4.8 CZTS Cells

Three cells were made to test the importance of the significance of the CZTS ratio as well as the ZnO HRT layer. These cells were made with a Mo thickness of 200 nm, CZTS thickness of 1.2±0.1 µm, 20 nm of CdS, and 150 nm of ITO. The sulfurization process varied between a hard anneal for 30 min or one for 60 min both at 510 °C. CELL1 was tested without the HRT ZnO layer, while CELL2 and CELL3 had 20 nm of ZnO. The parameters of the PV cells are shown in Table 7. Results show that the inclusion of the HRT ZnO layer improve the V_{oc} by approximately seven times and the I_{sc} by thirteen times. When the sulfurization time was increased to 60 min, CELL3, the performance of the cell dropped dramatically. This is due to the low zinc content of 2.8% in the CZTS layer from longer time exposures. CELL2 was chosen to be part of the MISSE-12 (Material Samples to be tested on the International Space Station) mission to be tested in a space environment.

Table 7 – CZTS PV Cells showing deposition parameters and performance characteristics. The CZTS ratio is defined as Cu(%), Zn(%), Sn(%), S(%).

	Sample	CZTS RATIO %Cu/%Zn/%Sn/%S	Anneal time	ZnO HRT	I_{SC}	V_{oc}	Sulfurization Recipe
	CELL1	20.6/14.2/47.7/17.5	30 min	No	957.8 nA	95 µV	Sulf_3
	CELL2	20.6/14.2/47.7/17.5	30 min	Yes	12.79 µA	680 µV	Sulf_3
	CELL3	21.1/**6.6**/47.7/24.6	60 min	Yes	922.8 nA	110 µV	Sulf_4

The IV curve of each is obtained using a Keithley SCS-4200 (Cleveland, OH) and an Oriel Sol3A solar simulator (Irvine, CA) illuminating at AM1.5, calibrated with a Newport 91150V (Irvine, CA). The performance of CELL2 is significantly better than the other cells (Figure 32). These cells performed poorly due to their incomplete CZTS stoichiometry. The fabricated cells are more of light reacting resistors rather than diodes.

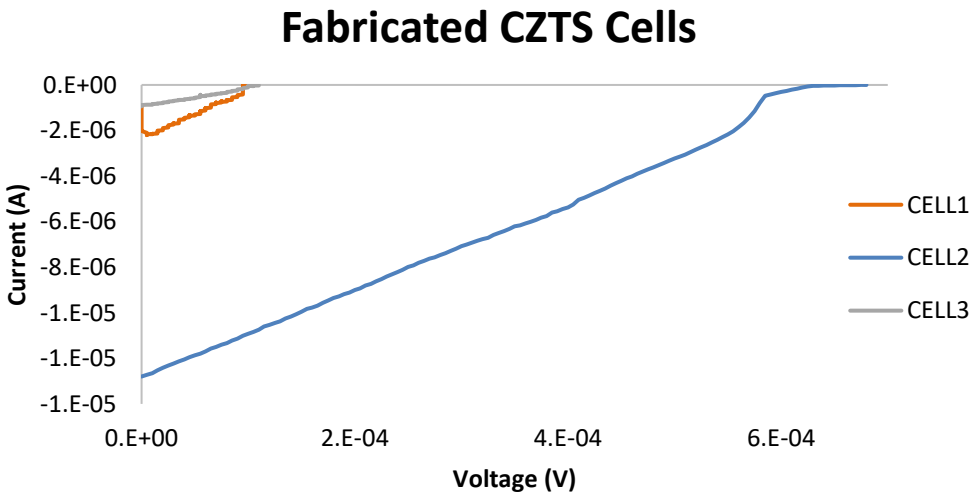

Figure 32 – IV curve of three CZTS PV cells.

4.9 Summary of Results

The fabrication process involved electron beam deposition of Mo as the back contact, sputtered CZT, plasma assisted H_2S sulfurization of CZT to create the p-type absorber layer CZTS, epitaxial growth of CdS as the n-type window layer, IAD of ZnO as the HRT passivation layer, and IAD ITO as the top contact.

The deposited Mo resulted in a uniform and smooth layer with sheet resistances of approximately 15.31 ± 0.2 Ω/□ for a thickness of 200 nm.

An acceptable method of sputtering 1.3 µm thick CZT was to cycle between deposition and cooling phases instead of a continuous deposition. The addition of cooling phases resulted in a denser and more uniform layer. This process resulted in a CZT layer with a composition of $Cu_{49.5}Zn_{27.5}Sn_{23}$ (atomic %).

A higher sulfurization anneal temperature of 575 °C results in holes with cracks on the surface that are rich in copper and sulfur. If the annealing time is too long, over 60 minutes, the sulfurized CZT will have a deficit of Zn. A lower sulfurization temperature resulted in surface extrusions that are tin and copper rich. When plasma was removed from the process, pinhole defects form on the surface. EDS analysis show that these defects are sulfur-rich, tin-poor, and copper-poor. The use of plasma seems to be crucial for creating CZTS with H_2S. Increasing the flow rate of H_2S results in an increase of sulfur content, though the zinc degradation is still present. A soft anneal step of 350 °C prior to the 510 °C hard anneal was shown to maintain the concentration of Zn in the sulfurized film. Higher processing pressure sulfurizations of 3×10^3 torr result in surface fissures. These fissures occur with and without a soft anneal step at high pressures.

The fabricated cells had very poor performance. This is due to the incomplete CZTS composition. The fabricated CZTS layer for these devices resulted in low zinc and sulfur content. Because of the incomplete composition of CZTS, the performance of the cells behave similar to light-reactive resistors instead of diodes. ZnO was shown to improve the performance of the device by approximately 6 times of the device without ZnO.

V SUMMARY AND FUTURE WORK

5.1 Summary of Contributions

This work focuses on developing fabrication processes that will be used towards creating CZTS PVs. The processes for the layers in the CZTS PV stack that are developed include electron beam deposition of Mo, sputtering CZT, sulfurization of CZT, and IAD of ZnO and ITO.

Additionally, this work also explores the use of plasma assisted H_2S in sulfurization of CZT to form CZTS. The use of plasma assisted H_2S to sulfurize CZT has been unexplored. Most sulfurization processes of CZTS utilizes a sulfur tube furnace [21, 49, 59, 60]. The data gathered from the sulfurization processes show that it may be possible to form CZTS using plasma assisted H_2S.

5.2 Future Work

Currently, the composition of deposited film by single target sputtering of CZT then sulfurization via H_2S plasma needs more sulfur. The CZT composition can be maintained in some sulfurization parameters, but there is an insignificant amount of sulfur within the film to be comparable to that of CZTS. There could be more parameters to change such as the power of the plasma and longer different sulfurization temperatures. Since a soft anneal of 350 °C results in adhesion problems, other temperatures may be explored. The hard anneal was chosen to be 510 °C, but may also change with soft annealing times.

A single CZTS target may be sputtered in a sulfur environment (H_2S flow while sputtering). The MBE tool used with these experiments has the capability to sputter in a sulfur environment, though there were some complications with the tool during the time of this research. It may be interesting to sputter CZT or CZTS in a sulfur environment.

The depositions of the other layers in the PV stack seem to have good results in terms of resistivity, uniformity, and transmittance. However, the transmittance of ITO can still be improved to reduce absorption losses. Factors such as changing the oxygen flow rate during the process, the oxygen flowing through the plasma ring, the deposition rate, and the plasma power may be further investigated to optimize the performance. Additionally, the thickness of Mo may also be varied to test the effectiveness of the out-diffusion of sodium into the absorber layer.

Finally, a light trapping structure, such as a textured surface, can be implemented in the design improve the efficiency. The planar CZTS PV stack may be deposited on top of a three-dimensional conductive material, such as patterned carbon nanotubes, to create a textured surface.

APPENDIX A. TABLES OF DEPOSITION PARAMETERS

A.1 Deposition of Mo

Table 8 – IAD deposition of Mo.

Name	Substrate	Tooling factor (%)	Set Thickness	Measured (nm)	Sheet Resistance (Ω/square)
TEST6	Si/glass	105.3	200 nm	211	56.051776
IAD_Mo__05nms_240_1	SLG/Si	113.7	240 nm	230-237 nm	-
IAD_Mo__05nms_200_2	SLG/Si	113.7	200 nm	195-200 nm	15.31816
IAD_Mo_3	2 SLG Wafers	113.7	200 nm	180 nm	19.338044

A.2 Deposition of CZT

Table 9 – Evovac CZT deposition parameters.

Sample Name	EV_TEST_CZ	EV_TEST_CZ	EV_TEST_CZ	EV_TEST_CZ	EV_TEST_CZ
Substrate	Si small piece	Si small piece	Si small piece	Si small piece	Si small piece
Rate (A/s)	0.1	0.8	1	0.8	1.9
Set Thick. (A)	200	1000	5000	5000	12000
Chamber	12	12	12	12	12
Power(%)	30	23	25	19	16.8
Power(W)	155+	136	167	116	100
Refl P (W)	2	2	6	1	0
P.I.D	60.5.0	60.5.0	60.5.0	60.5.0	60.5.0
Tooling %	36	36	36	36	100
Substrate	22	22	22	22	22
Meas. Thick.	-	-	-	200-300 nm	-
Composition	n/a	n/a	n/a	n/a	n/a
Denosition	Continu-ous	Continu-ous	Continu-ous	Continu-ous	Continu-ous

EV_TEST_CZ	EV_TEST_CZ	EV_TEST_CZ	EV_TEST_CZ	EV_TEST_CZ	EV_TEST_CZ	EV_TEST_CZ
Si 4" wafer	Si 4" wafer,	IAD #5 piece	IAD #5 piece	IAD_Mo_2	IAD_Mo_3	IAD_Mo_3
2	0.3	0.22	0.3-0.4	0.22-0.4	0.2	0.2-0.3
12000	3000	2000	2000	12000	13000	13000
12	12	12	4.2	1.8-4.2	4.2	4.2
16.9	22.6-24.5	23.5	22-24	20-24	17	17
101	130-150	142	130-142	144	100	100
0	1-3	1-2	1-2	0-1	0	0
30.3.0	30.2.0	30.2.0	30.2.0	30.2.0	30.2.0	30.2.0
100	13.75	12.14	12.14	12.14	12.14	12.14
22	150	100	150	150	150	150
165 nm	200-330 nm	176-231 nm	-	1.0-1.2 [um]	-	1.175.1.120.1.1
n/a	n/a	n/a	n/a	43.1.20.6.36.3	-	57.1.24.4.18.5
Continu-ous	Continu-ous	Continu-ous	Continu-ous	Continu-ous	Continu-ous	Cycled

A.3 Sulfurization of CZT

Table 10 – MBE sulfurization parameters.

Name	MBE_Sulf_1_57	MBE_Sulf_2_57	MBE_Sulf_3_40	MBE_Sulf_4_55	MBE_Sulf_5_57
Substrate	EV_TEST_CZT	EV_TEST_CZT	EV_TEST_CZT	EV_TEST_CZT	EV_TEST_CZT
Heater Temp	574	575	400,575	550	575
Heater voltage	33V, 5.06A	33V, 5.06A	33V, (3,71A,	33V, 4.863A	33V,5.06A
Time	30 min	30 min	30,30 min	60 min	30
idle Pressure	3.00E-04	3.00E-04	6.50E-06	2.50E-07	1.70E-07
process pressure	~3.00E-05	~3.00E-05	~3.00E-05	~3.00E-05	~3.00E-05
MFC N2 (sccm)	12.5	15.64	15.64	15.64	25
MFC H2S (sccm)	9.9875	12.5 (31.3%)	12.5 (31.3%)	12.5 (31.3%)	20 (50%)
EDS Composition	n/a	50.8,1,38.5,9.7	n/a	23.4,16.8,45.3,1	19.2,16.7,52.9,1

MBE_Sulf_6_51	MBE_Sulf_7_51	MBE_Sulf_8_51	MBE_Sulf_9_51	MBE_Sulf_10_5	MBE_Sulf_11_5
EV_TEST_CZT	EV_TEST_CZT	EV_TEST_CZT	EV_TEST_CZT	EV_TEST_CZT	EV_TEST_CZT
510	510	510	510	510	510
33V, 4.570A	33V, 4.570A	33V, 4.570A	33,4.573	33,4.573	33,4.573
30 min	15 min	30	30	30	60
7.50E-06	7.40E-06	2.00E-07	2.60E-07	2.60E-07	1.20E-07
~3.00E-05	~3.00E-05	~3.00E-05	~3.00E-05	3.00E-05	3.00E-05
15.64	15.64	15.64	15.64	15.64	15.64
12.5 (31.3%)	12.5 (31.3%)	12.5 (31.3%)	12.5 (31.3%)	12.5 (31.3%)	12.5 (31.3%)
20.6,14.2,47.7,1	25.3,14.3,52.8,7.	20.6,14.2,47.7,1	20.6,14.2,47.7,1	41.1,3.7,53.8,1.4	21.1,6.6,47.7,24.

MBE_Sulf_12_5	MBE_Sulf_13_5	MBE_Sulf_14_5	MBE_Sulf_15_3	MBE_Sulf_16_3	MBE_Sulf_17_3
EV_TEST_CZT	EV_TEST_CZT	EV_TEST_CZT	EV_TEST_CZT	EV_TEST_CZT	EV_TEST_CZT
510	510	510	(1) 350, (2) 510	(1) 350, (2) 510	(1) 350, (2) 510
33,4.573	33,4.573	33,4.573	33V, (1) 3.37A,	33V, (1) 3.37A,	33V, (1) 3.37A,
90	1 hr	1 hr	(1) 30 min, (2)	(1) 30 min, (2)	(1) 60 min, (2)
1.20E-07	1.20E-07	-	1.20E-07	1.20E-07	1.20E-07
3.00E-05	3.30E-05	5.20E-05	5.20E-05	5.20E-05	5.20E-05
15.64	15.64	43	43	43	43
12.5 (31.3%)	12.5 (31.3%)	86%	86%	86%	86%
18.5,2.8,46.3,32.	21.1,6.6,47.7,24.	55.5,0.5,9.5,34.5	45.7,22.3,18.2,1	27.5,36.0,11.8,2	37.2,30.6,15.4,1

MBE_Sulf_18_3	MBE_Sulf_19_5	MBE_Sulf_20_3	MBE_SULF_21
	EV_TEST_CZT	EV_TEST_CZT	EV_TEST_CZT
350	510	(1) 350, (2) 510	(1) 350, (2) 510
	33V, 4.570A	33V, (1) 3.37A,	33V, (1) 3.37A,
60 min	60 min	(1) 30 min, (2)	(1) 30 min, (2)
1.20E-07	-	1.30E-05	1.50E-05
5.20E-05	1.0-2.0E-3	1.0-5.0E-3	(1) 5.2E-4, (2)
43	15.64	43	1) 12.5. 2) 43
86%	31.30%	86%	1) 31.3% 2) 86%
47.5,26.2,18.8,7.	72.2,0,25.4,2.4	72.2,0,25.4,2.5	52.7,20.5,20.2,6.

A.4 MBE Deposition of CdS

Table 11 – MBE CdS deposition paramters.

Name	Subst-rate	Temp (°C) (CdS)	Temp (°C) (substr-ate)	Current stage	Time	BEP (Torr)	Thic-kness	Rate
MBE_CdS_650C_30min_1	Si	650	200	2.29 A	30 min	2.00E-07	na	na
MBE_CdS_475C_60min_2	Glass piece	475	200	2.29 A	1 hr	5.00E-09	na	na
MBE_CdS_700C_60min_3	Glass piece	700	200	2.29 A	1 hr	1.68E-06	125 nm	0.034 nm/s
MBE_CdS_790C_90min_4	Glass and Si	790	200	2.29 A	1.5 hr	3.01E-06	2.2-2.5 um	0.425 nm/s
MBE_CdS_824C_47s_5	MBE_Sulf_8_510C_30min	824	200	2.2 A	47s	3.00E-06	20 nm	0.425 nm/s
MBE_CdS_824C_48s_6	MBE_Sulf_9_510C_30min	830	200	2.2 A	48s	2.97E-06	23.66 nm	0.492 nm/s

A.5 MBE Deposition of ZnO

Table 12 – IAD ZnO deposition parameters.

Name	Subst-rate	Tooling factor (%)	Set Thick-ness (nm)	APS Bias Voltage (V)	Rate of deposi-tion	EBG emission current	GAS FLOW O2 (sccm)	Measured (nm)	4-pt probe Resistance (Ω)
IAD_ ZnO_2	slg piece and si	100	20	80	0.01 nm/s	21.3 mA	9	12.5, 17.148	>1MΩ
IAD_ ZnO_3	slg piece and si	100	50	80	0.01 nm/s	21.3 mA	9	44.48,50.25,52.45	>1MΩ

A.6 MBE Deposition of ITO

Table 13 – IAD ITO deposition parameters.

Name	Subst-rate	Tooling factor (%)	Set Thic-kness	APS Bias Voltage (V)	Rate of depos-ition	Subst-rate Temp (°C)	EBG emission current	GAS FLOW O2 (sccm)	Measu-red (nm)	4-pt probe Resist a-nce (Ω)
IAD_ITO_1	Si	100	80nm	85	0.01 nm/s	200	24 mA	9	32.46	-
IAD_ITO_2	Si + Glass	40.60%	80nm	85	<0.01 nm/s	200	24 mA	9	-	-
IAD_ITO_3	Glass + Si	32.5	3.74 nm	85	<0.01 nm/s	200	24	9	92	54.101 94175
IAD_ITO_4	Glass + Si	100	150	85	0.1 nm/s	200	35.5 mA	9	143	9.0026 47838
IAD_ITO_5	Glass + Si	95.3	150	85	0.2 nm/s	200	41 mA	9	150	60.657 54634
IAD_ITO_6	Glass + Si	95.3	5nm, 145nm	85	0.01nm/s, 0.05 nm/s	200	29.1, 33.2 mA	9	150	10.19
IAD_ITO_7	Glass + Si	95.3	5nm, 145nm	85	0.01nm/s, 0.1 nm/s	200	25.4, 35.5 mA	9	150	9.25
IAD_ITO_8	Glass + Si	95.3	5nm, 145nm	108.6	0.01nm/s, 0.1 nm/s	200	25.4, 35.5 mA	9	150	9.497

IAD_ITO_9	Glass + Si	95.3	5nm, 145nm	85	0.01nm/s, 0.1 nm/s	250	25.4, 35.5 mA	9	149.8	-
IAD_ITO_10	Glass + Si+MBE_CdS_824C_47s_5	95.3	5nm, 145nm	85	0.01nm/s, 0.1 nm/s	250	25.4, 35.5 mA	9	127.2	11.1
IAD_ITO_11	Glass + Si	95.3	5nm, 145nm	85	0.01nm/s, 0.1 nm/s	250	25.4, 35.5 mA	20	134.9333333	12.25
IAD_ITO_12	Glass + Si	85.7	5nm, 145nm	85	0.01nm/s, 0.1 nm/s	250	25.4, 35.5 mA	9	150	5.55
IAD_ITO_13	Glass + Si	77.13	5nm, 145nm	85	0.01nm/s, 0.1 nm/s	250	25.4, 35.5 mA	15	150	6.59

REFERENCES

[1] U. S. E. I. Administration. (2018, August 15). *What is U.S. electricity generation by energy source?* Available: https://www.eia.gov/tools/faqs/faq.php?id=427&t=3

[2] N. S. Lewis, "Research opportunities to advance solar energy utilization," *Science,* vol. 351, no. 6271, p. aad1920, 2016.

[3] REN21, "Renewable Energy Policy Network For The 21st Century," *Renewables 2018 Global Status Report,* no. 2018, 2018.

[4] J. Tsao, N. Lewis, and G. Crabtree. (2006). *Solar FAQs*. Available: www.sandia.gov

[5] B. Seger. (2016, September 16, 2018). *Global Energy Consumption: The Numbers for Now and In the Future*. Available: https://www.linkedin.com/pulse/global-energy-consumption-numbers-now-future-brian-seger

[6] E. Becquerel, "Memoire sur les Effets Electriques Produits sous l'Influence des Rayons Solaires " *Comptes Rendus,* vol. 9, pp. 561-567, 1839.

[7] L. M. Fraas, "History of Solar Cell Development," in *Low-Cost Solar Electric Power*Cham: Springer International Publishing, 2014, pp. 1-12.

[8] W. G. a. R. E. D. Adams, "The Action of Light on Selenium," *Proceedings of the Royal Society of London,* vol. 25, pp. 113-117, 1877.

[9] W. Smith, The Action of Light on Selenium, 1876. [Online]. Available.

[10] S. Klassen, "The Photoelectric Effect: Reconstructing the Story for the Physics Classroom," *Science & Education,* journal article vol. 20, no. 7, pp. 719-731, July 01 2011.

[11] M. A. Green, "Silicon photovoltaic modules: a brief history of the first 50 years," *Progress in Photovoltaics: Research and Applications,* vol. 13, no. 5, pp. 447-455, 2005.

[12] G. L. Pearson, "Conversion of Solar to Electrical Energy," *American Journal of Physics,* vol. 25, no. 9, pp. 591-598, 1957/12/01 1957.

[13] M. Courel, "Towards a CdS/Cu2ZnSnS4 solar cell efficiency improvement: A theoretical approach," *Applied Physics Letters,* vol. 105, no. 233501, 2014.

[14] J. Nelson, *The Physics of Solar Cells*. Imperial College Press, 2003.

[15] Y. Zhao *et al.*, *A solar photovoltaic system with ideal efficiency close to the theoretical limit*. 2012, pp. A28-38.

[16] A. Luque and S. Hegedus, *Handbook of Photovoltaic Science and Engineering*. Wiley, 2011.

[17] Y. R. Wu, C. Y. Huang, Y. Zhao, and J. S. Speck, "8 - Nonpolar and semipolar LEDs," in *Nitride Semiconductor Light-Emitting Diodes (LEDs)*, J. Huang, H.-C. Kuo, and S.-C. Shen, Eds.: Woodhead Publishing, 2014, pp. 250-275.

[18] M. A. Green, *Solar cells : operating principles, technology and system applications / Martin A. Green* (no. Accessed from https://nla.gov.au/nla.cat-vn1641381). Kensington, N.S.W: University of New South Wales, 1992.

[19] S. Kim, J.-S. Park, and A. Walsh, "Identification of Killer Defects in Kesterite Thin-Film Solar Cells," *ACS Energy Letters,* vol. 3, no. 2, pp. 496-500, 2018/02/09 2018.

[20] S. Siebentritt, "Why are kesterite solar cells not 20% efficient?," *Thin Solid Films,* vol. 535, pp. 1-4, 2013/05/15/ 2013.

[21] S. Zhuk, "Critical review on sputter-deposited Cu2ZnSnS4 (CZTS) based thin film photovoltaic technology focusing on device architecture and absorber quality on the solar cells performance," *Solar Energy Materials and Solar Cells,* vol. 171, pp. 239-252, 2017.

[22] T. Dhakal, "Characterization of a CZTS thin fim solar cell grown by sputtering method," *Solar Energy,* vol. 100, pp. 23-30, 2014.

[23] G. Conibeer, "Third-generation photovoltaics," *Materials Today,* vol. 10, no. 11, pp. 42-50, 2007/11/01/ 2007.

[24] A. O. P C Choubey, R Dewangan, "A review: Solar cell current scenario and future trends," *Recent Research in Science and Technology,* vol. 4, no. 8, pp. 99-101, 2012.

[25] M. A. Green, K. Emery, Y. Hishikawa, W. Warta, and E. D. Dunlop, "Solar cell efficiency tables (version 47)," *Progress in Photovoltaics: Research and Applications,* vol. 24, no. 1, pp. 3-11, 2016.

[26] G. P. Willeke, "Thin crystalline silicon solar cells," *Solar Energy Materials and Solar Cells,* vol. 72, no. 1, pp. 191-200, 2002/04/01/ 2002.

[27] P. Reinhard *et al.*, "Review of progress toward 20% efficiency flexible CIGS solar cells and manufacturing issues of solar modules," in *2012 IEEE 38th Photovoltaic Specialists Conference (PVSC) PART 2*, 2012, pp. 1-9.

[28] T. D. Lee and A. U. Ebong, "A review of thin film solar cell technologies and challenges," *Renewable and Sustainable Energy Reviews,* vol. 70, pp. 1286-1297, 2017/04/01/ 2017.

[29] D. E. Carlson and K. Rajan, "Hydrogen ion motion in amorphous silicon solar cells at elevated temperatures," *Applied Physics Letters,* vol. 69, no. 10, pp. 1447-1449, 1996.

[30] H. Katagiri, "Development of CZTS-based thin film solar cells," *ScienceDirect,* vol. 517, no. 7, pp. 2455-2460, 2009.

[31] K. Ramasamy, "Routes to copper zinc tin sulfide Cu2ZnSnS4 a potential material for solar cells," *ChemComm,* vol. 48, pp. 5703-14, 2012.

[32] R. Nakamura, "Cu2ZnSnS4 thin film deposited by sputtering with Cu2ZnSnS4 compound target," *Japanese Journal of Applied Physics,* vol. 53, no. 2S, 2014.

[33] H. Katagiri, K. Jimbo, M. Tahara, H. Araki, and K. Oishi, "The Influence of the Composition Ratio on CZTS-based Thin Film Solar Cells," *MRS Proceedings,* vol. 1165, pp. 1165-M04-01, 2009, Art. no. 1165-m04-01.

[34] C. J. Hages, M. J. Koeper, and R. Agrawal, "Optoelectronic and material properties of nanocrystal-based CZTSe absorbers with Ag-alloying," *Solar Energy Materials and Solar Cells,* vol. 145, pp. 342-348, 2016/02/01/ 2016.

[35] W. Wang *et al.*, "Device Characteristics of CZTSSe Thin-Film Solar Cells with 12.6% Efficiency," *Advanced Energy Materials,* vol. 4, no. 7, p. 1301465, 2014.

[36] C. Yan *et al.*, "Cu2ZnSnS4 solar cells with over 10% power conversion efficiency enabled by heterojunction heat treatment," *Nature Energy,* vol. 3, no. 9, pp. 764-772, 2018/09/01 2018.

[37] S.-F. Wang, "Characteristics of Bilayer Molybdenum Films Deposited Using RF Sputtering for Back Contact of Thin Film Solar Cells," *Advances in Materials Science and Engineering,* vol. 2014, 2014.

[38] Y. Kamikawa-Shimizu, "Effects of Mo back contact thickness on the properties of CIGS solar cells," *Physica Status Solidi,* vol. 206, no. 5, pp. 1063-1066, 2008.

[39] J. H. Scofield, "Sputtered molybdenum bilary back contact for copper indium diselenide-based polycrystalline thin- film solar cells," *Thin Solid Films,* vol. 260, pp. 26-31, 1994.

[40] J. L. Alleman, "Dependence of the Characteristics of Mo Films on Sputter Conditions," *National Renewable Energy Laboratory,* 2000.

[41] G. K. Dalapati, "Impact of molybdenum out diffusion and interface quality on the performance of sputter grown CZTS based solar cells," *Scientific Reports,* vol. 7, no. 1350, 2017.

[42] J. T. W. Jonathan Scragg, "A Detrimental Reaction at the Molybdenum Back Contact in Cu2ZnSn(S,Se)4 Thin-Film Solar Cells," *Journal of the American Chemical Society,* vol. 134, 2012.

[43] Z. Beqqali, Rogemond, "Electrical properties of molybdenum disulfide MoS2. Experimental study and density functional calculation results," *Synthetic Metals,* vol. 90, pp. 165-172, 1997.

[44] R. V. Forest, "Understanding the Role of Oxygen in the Segregation of Sodium at the Surface of Molybdenum Coated Soda-Lime Glass," *AlChE Journal,* vol. 60, no. 6, pp. 2365-2372, 2014.

[45] R. Thielsch, A. Gatto, J. Heber, and N. Kaiser, "A comparative study of the UV optical and structural properties of SiO2, Al2O3, and HfO2 single layers deposited by reactive evaporation, ion-assisted deposition and plasma ion-assisted deposition," *Thin Solid Films,* vol. 410, no. 1, pp. 86-93, 2002/05/01/ 2002.

[46] J. D. Plummer, M. D. Deal, and P. B. Griffin, *Silicon VLSI Technology: Fundamentals, Practice and Modeling*. Prentice Hall, 2000.

[47] P. J. Kelly and R. D. Arnell, "Magnetron sputtering: a review of recent developments and applications," *Vacuum,* vol. 56, no. 3, pp. 159-172, 2000/03/01/ 2000.

[48] H. Hiroi, "High Voltage Cu2ZnSnS4 Submodules by Hybrid Buffer Layer," presented at the Conference: 39th IEEE Photovoltaic Specialists Conference, Tampa, Florida, USA, 2013.

[49] Y.-P. Lin, "Preparation of Cu2ZnSnS4 (CZTS) sputtering target and its application to the fabrication of CZTS thin-film solar cells," *Journal of Alloys and Compounds,* 2015.

[50] H. Zhang, "Prospects of Zn(O,S) as an alternative buffer layer for Cu2ZnSnS4 thin-film solar cells from numerical simulation," *Micro & Nano Letters,* vol. 11, no. 7, pp. 386-390, 2016.

[51] S. K. B. Goutam Kumar Dalapati, Seid Masudy-Panah, "Sputter grown sub-micrometer thick Cu2ZnSnS4 thin film for photovoltaic device application," *Materials Letters,* vol. 160, pp. 45-50, 2015.

[52] L. S. Jun He, Kezhi Zhang, "Effect of post-sulfurization on the composition, structure and optical properties of Cu2ZnSnS4 thin films deposited by sputtering from a single quaternary target," *Applied Surface Science,* vol. 264, pp. 133-138, 2013.

[53] U. Obahiagbon, "The role of the intrinsic zinc oxide layers on the performance of wide-bandgap (AgCu)(InGa)Se2 thin-film solar cells " presented at the 2015 IEEE 42nd Photovoltaic Specialist Conference (PVSC) New Orleans, LA, USA 2015.

[54] X. L. F.S. Hasoon, A. Kanevce, C. Perkins, S. Asher, H.A. Al- Thani, "Investigation of the Effect of I-ZnO Window Layer on the Device Performance of the Cd-Free CIGS Based Solar Cells " presented at the Photovoltaic Specialists Conference 33rd IEEE,, 2008.

[55] J. William D. Callister, *Fundamentals of Materials Science and Engineering*, 5 ed. John Wiley & Sons, Inc., 2001.

[56] G. M. Swain, "Solid Electrode Materials," *Handbook of Electrochemistry,* 2007.

[57] J. Flicker, "Three-Dimensional Carbon Nanotube Based Photovoltaics," Doctor of Philosophy, School of Materials Science and Engineering, Georgia Institute of Technology, Georgia Institute of Technology, 2011.

[58] C. Perini, "Impact of As-synthesized and Radiation-induced Defects in Two-dimensional Vertical Heterostructures," Doctorate, School of Materials Science and Engineering, Georgia Institute of Technology, Georgia Institute of Technology, 2019.

[59] H. Araki *et al.*, "Preparation of Cu2ZnSnS4 thin films by sulfurization of stacked metallic layers," *Thin Solid Films,* vol. 517, no. 4, pp. 1457-1460, 2008/12/31/ 2008.

[60] A. Khalkar, K. Lim, S. Yu, J. H. Kim, and J. Yoo, "Sulfurization approach using sulfur vapor, graphite box and H2S gas atmospheres for co-sputtered Cu2ZnSnS4thin film," in *2014 IEEE 40th Photovoltaic Specialist Conference (PVSC)*, 2014, pp. 0390-0394.